INITIAL ASSESSMENT OF SURFACE PRESSURE CHARACTERISTICS OF TWO ROTARY WING UAV DESIGNS[*]

Henry E. Jones
Oliver. D. Wong
U.S. Army Aeroflightdynamics Directorate
AMRDEC, U. S. Army Research & Development Command

A. Neal Watkins
NASA Langley Research Center

Kevin W. Noonan
Deane G. Reis
Brendon D. Malovrh
U.S. Army Aeroflightdynamics Directorate
AMRDEC, U. S. Army Research & Development Command

Joanne L. Ingram
Swales Aerospace

Abstract

This paper presents results of an experimental investigation of two rotary-wing UAV designs. The primary goal of the investigation was to provide a set of interactional aerodynamic data for an emerging class of rotorcraft. The present paper provides an overview of the test and an introduction to the test articles, and instrumentation. Sample data in the form of fixed system pressure coefficient response to changes in configuration attitude and flight condition for both rotor off and on conditions are presented. The presence of the rotor is seen to greatly affect the magnitude of the response. Pressure coefficients were measured using both conventional pressure taps and via pressure sensitive paint. Comparisons between the two methods are presented and demonstrate that the pressure sensitive paint is a promising method; however, further work on the technique is required.

Introduction

Unmanned Aerial Vehicles (UAV) are remotely piloted or self-piloted aircraft that can carry a variety of payloads and weapons. The wide range of UAV missions require engineering assessments, which must be accomplished by a combination of theoretical, experimental (including wind tunnel and flight test), and computational techniques. Experimental data, in particular, will enhance the ability to support the timely and cost effective development of these and other emerging systems. One of the most critical areas of flight vehicle development is the aerodynamic technologies that deal with the airframe, in particular, the mitigation of adverse aerodynamic forces. These forces include drag, interactional effects such as tail buffet, Reynolds number effects, and the effect of stores on overall aerodynamics. In spite of this need, there appears to be a lack of experimental data to support these developing systems, especially for rotorcraft applications.

For this reason, an experimental investigation of two rotary-wing UAV designs was conducted. The primary goal of the investigation was to provide a set of interactional aerodynamic data for an emerging class of rotorcraft. A supporting goal was to ensure that the geometries employed were readily accessible for easy modeling in available CFD codes. These designs were developed in-house and are based on two generic cross section shapes; a hexagonal shape (Hex Model) and a triangular shape (Tri Model). The designs are 26.5% scale representatives of an envisioned 3500lb aircraft. The test involved a parametric study of the affect of fuselage shape, rotor presence, wing lift and drag, and store configuration on the fixed and rotating system forces and moments. Pressure coefficient data were also taken on both configurations using pressure sensitive paint on the fuselage upper surface. In addition, static pressure coefficients were measured on the Hex body using conventional pressure taps. Both configurations were instrumented with a set of four of dynamic pressure taps which were used primarily to calibrate the pressure sensitive paint measurements. Because of the large body of data taken, a complete discussion of the entire test is beyond the scope of a single paper. A general introduction to the test and force data is presented in Ref. 1. For completeness, the present paper also provides a review of the test and an introduction to the test articles, and instrumentation. However, the sample data presented here will focus on the fixed system pressure coefficient response for both rotor on and rotor off conditions as measured by both ESP and PSP methods.

Symbols and Abbreviations

A	reference area (27.57), ft^2
c	wing chord, ft
C_D	drag coefficient (D/qA)
C_L	lift coefficient (L/qA)
C_P	pressure coefficient $\quad (p - p_\infty)/q$
D	drag, lb
L	lift, lb
q	dynamic pressure, (1/2) ρV^2, lb/ft^2
S	surface wetted area, ft^2
V	free stream velocity, ft/sec
α	Angle of attack, deg
β	Angle of sideslip, deg
α_{wing}	Wing angle of attack, deg
ρ	Density of air, slugs/ft^3

Abbreviations

Hex	hexagonal-shaped body
Tri	triangular-shaped body
ESP	electronically scanned pressures
IRTS	isolated rotor test system
KTAS	knots, true air speed
LVDT	linear variable differential transformer
MPA	model preparation area
PSP	pressure sensitive paint

Apparatus and Models

The 14X22 Tunnel

The Langley 14-by 22-Foot Subsonic Tunnel is an atmospheric, closed return tunnel with a test section 14.5-ft high, 21.75-ft wide, and 50-ft long which can reach a velocity of 348 ft/sec with a dynamic pressure of 144 psf (Ref. 2). The Reynolds number per foot ranges from 0.0 to 2.2 x10^6. The flow in the closed test section configuration is relatively uniform with a velocity fluctuation of 0.1 percent or less. Test section airflow is produced by a 40-ft diameter, nine-bladed fan. The tunnel has a set of flow control vanes to maintain close control of the speed for low-speed testing. Model force and moment measurements are typically made with six-component strain-gage balances.

For the present effort, the Isolated Rotor Test System (IRTS) was used to power the rotor. The IRTS consists of a drive motor, balance, and controls for a single rotor. The components are stacked in a linear fashion to provide minimal obstruction to the flow into and out of the rotor disk. A sketch of the IRTS and the model set-up is presented in Fig. 1. The IRTS is mounted to the non-flow side of the test- section ceiling. The base supports an arc sector to vary the angle of attack of the entire drive system (including the rotor shaft) while maintaining the center of the rotor near the centerline of the test section. A 50 hp electric motor is attached to the arc sector. Power from the motor is transmitted to the drive shaft by way of two drive belts. A 36 channel slip ring is installed at the base of the shaft to transfer electrical signals from the rotating to the non-rotating system. The hollow drive shaft is supported within a stepped cylinder that forms the external surface of the IRTS. The drive shaft passes through the rotor balance. Electric actuators control a swash plate for rotor collective and cyclic pitch. The end of the drive shaft is designed to accept hubs from the two-meter rotor test system (Ref. 3). For this test a similar four-bladed, fully articulated hub was used.

Fuselage Models

One of the primary goals of the present effort is to provide a data set which can be used in CFD code validation and calibration. Developing a geometric model of a configuration (i.e. a grid) is the most

important first step in any CFD analysis. The fuselage model design process used in the present case was developed in order to insure that each of the basic fuselage shapes were geometrically simple, generic and, most importantly, analytically or numerically defined. Using analytically or numerically defined shapes ensures that each basic geometry is readily accessible and hence, easy to grid. Employing generic shapes ensures that the data set is unrestricted and, hence available to a broad number of CFD code developers.

The model configurations chosen belong to a family of nine shapes which are designed based on three cross sections (triangle, hexagonal, and oval) and three longitudinal shape functions (symmetric, convex, and conventional). Details of the design process may be found in Ref. 1. Two of the nine fuselage model configurations were selected to be tested; a hexagonal shape (Hex Model, Fig. 2.) and a triangular shape (Tri Model, Fig. 3.).

Wing Model

A wing was designed along with these configurations in order to explore the effects of wing lift on configuration aerodynamics and to provide mount points for rockets. As with the fuselage shapes, the wing was designed to be a simple geometric shape in order to ensure ease of modeling. The wing layout was developed by following the description presented by Stepniewski (Ref. 4) and using the Apache wing geometry as a guide. Further details of the wing design may be found in Ref. 1.

Rotor Model

The rotor used for this test is a representative modern rotor design with a radius of 35.30 in., a nonlinear twist, and a set of modern airfoils. The flapping and lag hinges are coincident at the 2.00 in. radial station. The rotor blades used in this test have a tapered planform with a chord of 2.25 inches. The root cutout is approximately 17 percent of the radius. Further details of the rotor are listed in Table 1, which is taken from Ref. 5. Note that the radius of the hub used in the current effort is 0.25 in. shorter than the one used in Ref. 5. For the current effort the rotor lift coefficient was set to 0.006 for the entire test.

Force Measurement Instrumentation

Fuselage forces and moments were measured using a conventional six-component strain gage balance.

Rotor forces and moments were measured with a five-component strain gage balance installed in the IRTS. The rotor balance measured the force in each of the three coordinate directions and the pitching and rolling moments referenced approximately the center of the rotor hub. Rotor torque was measured with two redundant strain gage bridges on the rotor shaft. Rotor shaft angle was measured using an accelerometer with an accuracy ±0.01°. Actuator extension for the rotor controls was measured using a redundant system of linear variable displacement transducers (LVDTs) and encoders. These outputs were resolved into rotor collective pitch, longitudinal cyclic pitch, and lateral cyclic pitch. Assumed accuracies of the control positions are ±0.5°, based on the hysteresis of the calibrations at the maximum angles (worst case). Hall Effect devices were installed on the flapping and lagging hinges to measure the motion of the reference blade. Rotor rotational speed and reference blade azimuthal position were measured using optical encoders. For the 0° azimuthal position, the reference blade 1/4 chord was located over the tail.

Test

The test matrix was principally a study of the effect of a systematic variation of configurations and flight conditions on the fixed system aerodynamic forces and pressures. Flight conditions were varied using a set of four sweeps as displayed in Table 2. Details of the sweep variation may be found in Ref. 1. The present paper will focus on the pressure coefficient response observed during the alpha, beta, and speed sweeps.

Alpha variations ranged from -9 to 0 deg. in 3 deg increments. During alpha sweeps with the rotor present, the IRTS rotor shaft was pitched with changes in fuselage α so that the rotor shaft was kept perpendicular to the body waterline. Beta variations ranged from -16 to + 16 degrees in 2 deg. increments for rotor off and 4 deg. increments for rotor on. Speed sweeps capture the effect of velocity on the body forces and pressures. Speeds of 40 to 160 knots in increments of 20 knots were employed to achieve this.

Pressure Coefficient Measurements

The present test articles feature an extensive set of pressure instrumentation and measurements. The test featured an exploratory investigation of the use of pressure sensitive paint (PSP) to take model surface

$$\frac{I_{REF}}{I} = A(T) + B(T) \frac{P}{P_{REF}}$$

where I_{REF} is the recovered luminescence intensity at a reference pressure, P_{REF}. The most common method for PSP data acquisition is a "steady-state" mode in which I_{REF} is typically acquired while the wind tunnel is off or at very low speed and P_{REF} is the static pressure when no wind is applied. Thus I_{REF} is referred to as the "wind-off" intensity and I the recovered luminescence intensity at some pressure P. Since these data are collected at a specific condition in the wind tunnel, It is also referred to as the "wind-on" intensity. A and B are temperature dependent constants for a given PSP formulation and can be determined using either an *a priori* calibration (using laboratory-based calibration instrumentation), or an *in situ* calibration (calculating A and B based on comparison with pressure taps existing in the model), or a combination of the two calibration methods.

The PSP formulation used in this test consisted of the luminophore platinum (II) meso-tetra (Pentafluorophenyl) porphine, (PtT (PFP) P for short) dissolved in a fluoroethylmethacrylate-based polymer binder (FEM). The UAV models were prepared by first applying a basecoat consisting of white epoxy paint. This served to hide imperfections in the model surface as well as enhance adherence of the PSP layer. A layer of PtT (PFP) P/FEM containing titanium dioxide (TiO_2) was applied to the model followed by an overspray of PtT (PFP) P/FEM. After allowing the PSP layer to cure, registration marks were applied to the model and the three-dimensional coordinates of the marks were measured relative to the model coordinate system using a Faro Arm Coordinate Mapping Machine.

Illumination of the paint was accomplished using custom-made lamps based on 395 nm light emitting diodes (LEDs). The wavelength of the LEDs is very close to the absorption maximum of the PtT (PFP) P ensuring the brightest emission from the paint. Additionally, the LEDs can be pulsed as fast as 10 µsec at rates up to 5 kHz, effectively freezing the rotation of the blades. Emission from the paint was captured using two back-lit, slow-scan, scientific grade CCD cameras (16-bit and 14-bit digital resolution). Bandpass filters centered on the emission wavelength of the PtT (PFP) P (650 nm) were attached to each camera to reduce stray light and residual LED illumination. PSP images were acquired by either operating the LED lamps at a rate of 5 kHz (when no blades were present), or controlled using a programmable logic controller (LabSmith LC880) and pulse generator (Stanford Research System DG535) triggered from an optical encoder built into the rotor system. For acquiring wind-off images when the rotor was present, the rotor was operated at a "slow-roll" speed of 220 rpm with

---

pressures for both the Hex and Tri configurations. Conventional pressure tap technology in the form of an Electronically Scanned Pressure (ESP) system was employed on the Hex model to provide a reliable method to compare with the PSP method. The limited number of taps on the model precludes any direct comparison with force data; however, there are a sufficient number of points to provide an overall picture of the body response. Furthermore, there is more than enough data to provide support for correlation with CFD codes

Electronically Scanned Pressures

Electronically-scanned pressure systems provide a low-cost-per channel instrumentation solution where large numbers of pressure measurements are required. These systems are computer controlled; they are relatively easy to use; they provide on demand, calibration techniques; and, they are capable of high accuracy. Their miniature, high transducer-density design permits placement of these scanners in space-limited locations (e.g. inside wind-tunnel models). For the current test, 277 pressure ports were employed on the Hex model. The taps are arranged in 22 rings of 10 to 14 taps arranged around the circumference of the model. Fig. 4 shows the distribution of these taps. Accuracy for these transducers is $\pm$ 0.042 C_P.

Pressure Sensitive Paint

While ESP systems provide a reliable and accurate method of assessing the pressure response of a model, they contain two inherent drawbacks. The first is the discreet nature of the system which is incapable of capturing all of the details of the surface response. The second is the cost and complexity of including pressure ports on the model and the interior tubing necessary to support the pressure sensors. For these reasons, an exploratory application of pressure sensitive paint technology was used during the test to both develop and assess this emerging method.
PSP measurements exploit the oxygen (O_2) sensitivity of luminescent probe molecules suspended in gas-permeable binder materials. If the test surface under study is immersed in an atmosphere containing O_2 (e.g. air), the recovered luminescence intensity can be described by a modified Stern-Volmer relationship

no forward tunnel speed. All data analysis was performed using custom PSP analysis software (Greenboot, NASA Ames Research Center) and *in situ* calibration of the paint was performed using existing pressure taps. Figure 5 shows the arrangement of the lights and camera in the test section

Discussion of Results

Presentation of the complete data set is beyond the scope of this paper; however a representative selection of data from the test is included in figures 8 through 35. Figures 8 through 27 present data taken on the Hex model using the ESP system, while figures 28 through 35 present pressure sensitive paint measurements for both configurations.

ESP Pressure Coefficient Data

ESP pressure coefficient data are presented as a function of fuselage butt-line for several body stations. Figure 6 presents the distribution of taps for the butt-line format which includes crossections at body stations X= 1.96, 11.69, and 42.88. Figure 7 presents the distribution of taps for the body station format which includes a line of taps along the port side of the body just inboard of the chine and on the upper surface. Tables 3 and 4 give the exact locations of these taps. All of the ESP data presented are for the full configuration (i.e. body + wing + both rockets) unless otherwise noted.

Variation of Pressure Coefficient with Angle of Attack

Figures 8 through 13 present the variation of pressure coefficient on the body as a function of angle-of-attack. Figures 8-10 present the data for rotor off, and figures 11-13 present rotor on data. All of these data were taken at a speed of 100 KTAS and zero yaw angle on the body. Angles-of-attack were measured from 0.0 to -9.0 deg. in 3 deg. increments.

Figure 8 presents pressure coefficients at the body nose (X = 1.96). As might be expected, the upper surface pressure coefficients are positive since this is near the nose stagnation point. Lower surface pressure coefficients are also positive except for the few that are close to the body centerline. Pressure coefficients range from approximately 0.2 at 0 deg., to approximately 0.6 at -9 deg on the upper surface, and from approximately -0.3 to 0.2 on the lower surface. There is an asymmetry in the pressure

coefficients with starboard side (Y positive) of the body showing higher pressure coefficients. Figure 9 presents pressure coefficients just in front of the pylon (X = 11.69). At this point, a considerable expansion has taken place and pressure coefficients at the body centerline have dropped to $\pm$ 0.1. Pressure coefficients at the chine have dropped to values of approximately -0.25 to approximately -0.20, and are only weakly dependent on angle-of-attack. Lower surface values range from approximately -0.1 to -0.5 depending on angle-of-attack. The asymmetry in pressure coefficient remains. Figure 10 presents the pressure coefficient on the aft body just behind the pylon (X = 42.88). At this point, the expansion has completed and the pressure coefficients are uniformly low at approximately -0.3, and only weakly dependent on angle-of-attack.

Figures 11, 12, and 13 present pressure coefficients at the same body locations and test conditions as shown in figures 8, 9, and 10, however, here, the rotor is on. In Figure 11, the nose region, the pressure coefficient response with the rotor is very similar, in form, to the rotor off condition but with noticeably higher pressure coefficients on the upper surface. Lower surface pressure coefficients appear to have increased in magnitude also but to a somewhat lesser extent. Figure 12, just in front of the pylon, shows a very strong effect due to the rotor on the upper surface pressure coefficients. There is a jump in peak pressure coefficients from approximately 0.1 to approximately 0.3 (at -9 deg.) with a clear angle-of-attack trend. Chine pressure coefficients collapse to approximately -0.2 on the port side and to -0.1 on the starboard side, thereby increasing the asymmetry of loading. Figure 13, aft of the pylon, is very similar to Fig. 10, with pressure coefficients collapsing to approximately -0.3, but with slightly more variation due to angle-of-attack.

Variation of Pressure Coefficient with Yaw Angle

Figures 14 through 19 present the variation of pressure coefficient on the body as a function of yaw angle. Figures 14-16 present the data for rotor off, and figures 17-19 present rotor on data. All of these data were take at a speed of 100 KTAS and zero angle-of-attack on the body. Yaw angles were measured from -16 deg to + 16 deg in 2 deg increments for rotor off and 4 deg increments for rotor on. Data are presented herein at -16 to + 16 in 8 deg increments for both conditions.

Figure 14 presents pressure coefficients at the body nose (X = 1.96). As, with the angle-of-attack data

(Fig. 8), upper surface pressure coefficients are positive since this is near the nose stagnation point. Unlike the conditions in Fig. 8, however, the lower surface pressure coefficients are also all positive. Pressure coefficients range from approximately 0.1 at 16 deg. to approximately 0.7 at -16 deg on the port side chine. The starboard chine pressure coefficients range from approximately 0.15 to approximately 0.75 for the same yaw angles. Figure 15 presents pressure coefficients just in front of the pylon (X = 11.69). Again, as with the angle-of-attack data (Fig. 9), a considerable expansion has taken place and peak positive pressure coefficients at the body centerline have dropped to approximately -0.1 to 0.0 depending on yaw angle. Pressure coefficients at the chines show a strong variation with yaw and range from approximately 0.0 to approximately -0.35. Lower surface pressure coefficients are close to the upper surface values and reflect the zero angle-of-attack condition and the general symmetry of the model. Figure 16, aft of the pylon, shows the same general drop in the magnitude of the pressure coefficients seen in the angle-of-attack plots (Fig. 10), though, there is a much higher sensitivity to yaw angle.

Figures 17, 18, and 19 present pressure coefficients at the same body locations and test conditions as shown in figures 14, 15, and 16; however, here, the rotor is on Fig. 17 (X=1.96) shows somewhat higher pressure coefficients on the upper surface when compared to the rotor off condition (Fig. 14). In Fig. 18 (X=11.69), pressure coefficients have increased sharply on the upper surface and with little change to the lower surface when compared to the rotor off condition (Fig. 15). Fig. 19 (X=42.88) also shows higher pressure coefficients compared to the rotor off case (Fig. 15).

Variation of Pressure Coefficient with Speed

Figures 20 through 27 present the variation of pressure coefficient on the body as a function of speed. All of these data were taken with the body at zero angle-of-attack and yaw. Speed was varied from 60 KTAS to 140 KTAS in 20 knot increments.

Figure 20 presents pressure coefficients at the body nose (X = 1.96). The span-wise variation in pressure coefficient is seen to vary from approximately 0.42 on the port chine to approximately .50 on the starboard chine. There is some variation between the upper and lower surfaces with a delta C_P of approximately 0.1 in the middle of the body and the pressure coefficient difference collapsing near the chines. Figure 21 shows the pressure coefficients ahead of the pylon (X = 11.69). Here, the pressure

coefficients have dropped to approximately -0.2 at the chines and to zero in the middle of the span. Upper and lower surface pressure coefficients are very close. Figure 22 shows the aft of the pylon region (X = 42.88) with the pressure coefficients collapsing to near -0.3 across the span. For rotor off conditions and with no variation in either angle-of-attack or yaw, the pressure coefficient response of the body is seen to be independent of velocity (as expected). Comparisons of pressure coefficient distributions between figures 8, 9, and 10(at $\alpha = 0$) and those in figures 20, 21, and 22 show identical results for these conditions.

Figures 23, 24, and 25 present pressure coefficients at the same body locations and test conditions as shown in figures 20, 21, and 22; however, here, the rotor is on. Figure 23 (X = 1.96) shows higher pressure coefficients on the upper surface when compared to the rotor off case (Fig. 20). The largest difference occurs at 60 KTAS and the effect tapers off with increased speed. Figure 24 (X = 11.69) has sharply higher pressure coefficients on the upper surface than those seen in Fig. 21. Lower surface, pressure coefficients are largely unchanged compared to Fig.21. Again, these effects are higher at low speed and drop off as speed increases. Figure 25 (X = 42.88) shows a larger variation of pressures in this region of the body as compared to the variation due to alpha and beta (Fig. 13 and Fig. 19) again with low speed having the highest impact.

Figure 26 presents a plot of upper surface pressure coefficient vs. body length for rotor off conditions for various forward speeds. The figure shows a sharp decrease in pressure coefficient after the leading edge peak followed by a gradual decrease until just behind the pylon. This is followed by a rise in pressure coefficient as the flow turns toward the tail boom. Along the length of the tail boom, the flow gradually returns to free stream value. The rotor off condition presented here shows almost no variation in pressure coefficient with speed. Note that lower surface pressure coefficients are omitted here since they are very close to the corresponding upper surface values.

Figure 27 presents a plot similar to Fig. 26 but with rotor on conditions added. The single rotor off curve shown on Fig. 27 is taken from Fig. 26 (the 60 KTAS condition). The trend with speed shown in this figure shows the highest pressure coefficients occurring at low speed, 60 KTAS and as speed increases, the pressure coefficients gradually decrease to values near those of the no rotor condition. These results imply a strong wake downwash effect on the body which tapers off with increased speed.

PSP Pressure Coefficient Data

PSP pressure coefficient data are presented as a function of fuselage butt-line and also in the form of contours on the body for both the Hex and Tri models. All of the PSP data presented are for the basic configuration alone without the rotor.

PSP Surface Pressure Coefficient Contours

Figures 28 and 29 show surface contours of pressure coefficient on the Hex and Tri bodies respectively for a speed of 100 KTAS and $\alpha=\beta=0^{o}$. A qualitative comparison of Fig. 28 (Hex model) with figures 8, 9, and 10 shows fair correlation between the two techniques. Of particular interest is the indicated asymmetry in loading between port and starboard sides of the body, which was also seen in the ESP data and the loads data presented in Ref. 1. Figure 29 (Tri model) reveals a much more uniform pressure coefficient distribution on this body and generally lower values i.e., less negative pressure coefficient. It should be noted that the broad "strips" of uniform color on each of these figures are caused by the model tape and should not be confused with actual data.

Figures 30 and 31 show a comparison of ESP and PSP measurements at the same two body stations on the Hex model for two different angles of attack. These comparisons show a qualitative correlation between the two approaches, however better quantitative results over a wide range of conditions must await further development of the technique.

Nitrogen Tracer Surface Visualization

In addition to the surface pressure coefficient data, a novel flow visualization technique was explored to gain insight into surface flows. Data from this technique is presented for rotor on conditions for the Hex model. The method involves removing the pressure instrumentation from the body and replacing it with a system which pumps nitrogen through the pressure tubing system and onto the surface. The method exploits the fact that the PSP paint is sensitive to the presence of oxygen as explained above. The presence of nitrogen on the body surface displaces oxygen in the local flow and thereby increases the luminescence of the paint. The resulting images are surface streak lines.

Figures 32 through 35 present the results of these nitrogen tracer measurements along with force data with which to compare. Figure 32, taken from Ref. 1, presents the variation of lift coefficient with speed for rotor on and off conditions for both (Tri and Hex) basic configurations. Note in particular the large download on both models caused by the presence of the rotor. The load is highest at low speed and tapers off as forward speed increases. Figures 33 through 35 show surfaces images of the Hex model taken at 36, 60, and 136 KTAS. The surface streak lines show a strong downwash presence at low speed which tapers off at the higher forward speeds and is consistent with the force data presented in Fig. 32.

Assessment of PSP Results

As shown in Figs. 30 and 31, comparisons between the ESP data and the pressure coefficients determined from pressure sensitive paint show *qualitative* agreement, yet there is a consistent difference between the PSP data and the ESP data. This is a common effect observed during low speed testing in an ambient environment where overall pressure changes on a model surface are typically small (~0.2 psig or less). Because of the mechanism of PSP, at high pressures (e.g. near ambient), the sensitivity (intensity change as a function of pressure) of the PSP decreases, causing other experimental and environmental factors (e.g. temperature changes between wind on and wind off images, lighting instability, electronic noise from cameras, etc.) to degrade the accuracy of the measured PSP response. These effects are only partially overcome by calibrating against existing pressure taps (in situ calibration), and the error will generally increase on areas of the model where taps do not exist. Reducing these errors will greatly improve *quantitative* results from the PSP as well as minimize (though probably not completely eradicate) the need for using discrete pressure sensors or transducers.

Conclusion

A wind-tunnel test on two rotary-wing UAV designs has been completed. Hex model pressures were measured over a wide range of flight speed and body angle using standard ESP methods. Use of a pressure sensitive paint (PSP) technique was explored to measure data for both configurations. The following observations can be made based on the data presented herein:

1. The rotor wake has a significant affect on body pressure coefficients.
2. Trends observed in the pressure coefficient data measurements correlate with observed

trends in the force data as reported in a previous paper.

3. Asymmetric loads are observed in pressure coefficient data.

4. PSP data measurements show promising qualitative correlation with ESP data.

5. Flow visualization images support rotor download trends observed in the force data.

References

1. Jones, H. E., Wong, O. D., Noonan, K. W., Reis, D. G., and Malovrh, Brendon D. "Aerodynamic Characteristics of Two Rotary Wing UAV Designs," AHS International Vertical Lift Aircraft Design Conference, San Francisco, CA. January 2006.

2. Gentry, G. L.; Quinto, P. F.; Gatlin, G. M.; and Applin, Z. T.: "*The Langley 14- by 22-Foot Subsonic Tunnel: Description, Flow Characteristics, and Guide for Users"*. NASATP 3008, 1990.

3. Phelps, A. E., and, Berry, J. D., "*Description of the Army's 2-Meter Rotor Test System"*. NASA TM-87762, AVSCOM TM-86-B-4, 1987.

4. Stepniewski, W. Z., Keys, C. N., Rotary-Wing Aerodynamics, Dover Publications, Inc., New York, 1984.

5. Gorton S.A., Berry J.D., Hodges W.T., and Reis D.G.: *Flow Environment Study Near the Empennage of a 15-Percent Scale Helicopter Model*, NASA/TP-2000-210085

Tables

Table1. Description of Rotor.

Airfoil section		Number of blades 4
23.7 percent radius VR-12		Pitch axis, percent of chord 25
84.6 percent radius VR-12		Radius, in. 35.30
91.8 percent radius SSC-A09		Solidity, thrust-weighted 0.0787
100 percent radius SSC-A09		Tip sweep angle of quarter chord, deg 30
Chord, in.		Tip sweep begins in. 31.45
23.7 percent radius 2.25		Twist deg
84.6 percent radius 2.25		0 percent radius 0
91.8 percent radius 2.25		23.7 percent radius 0
100 percent radius 1.35		74.3 percent radius .... -6.6
Cutout, in. 8.2		84.6 percent radius .... -7.6
Flapping hinge offset, in. 2.0		91.8 percent radius .... -9.5
Lag hinge offset, in. 2.0		100 percent radius .... -9.5

Table 2. Test Conditions.

Data Set	Data Range	Hex	Tri
Trim Sweep	$40 \rightarrow 140$ KTAS ($\alpha = 0 \rightarrow -5.5$, $\beta = 0$)	X	X
Alpha Sweep	$0 \rightarrow -9$ deg @ 100 KTAS ($\beta = 0$)	X	X
Beta Sweep	$-16 \rightarrow 16$ @ 100 KTAS ($\alpha = 0$)	X	X
Speed Sweep	$40 \rightarrow 140$ KTAS ($\alpha = \beta = 0$)	X	X

Table 3. Pressure tap locations for station plots

SL = 1.96			SL = 11.69			SL = 42.88		
X	Y	Z	X	Y	Z	X	Y	Z
1.9587	1.5077	1.9517	11.6902	1.4944	4.3964	42.8810	7.0583	4.0105
1.9410	4.3125	1.0246	11.6935	6.9754	4.0186	42.8767	10.1733	2.0219
1.9538	5.4739	0.2933	11.6927	10.0930	2.0184	42.8933	12.8775	0.2813
1.9472	4.3059	-1.0697	11.7102	12.8338	0.2742	42.8718	10.1741	-2.0657
1.9285	1.4978	-1.9817	11.6723	10.0828	-2.0598	42.8578	7.0573	-4.0532
1.9472	-1.4915	-1.9761	11.6984	6.9606	-4.0564	42.8760	-7.0583	-4.0420
1.9451	-4.3019	-1.0473	11.6647	1.4945	-4.4064	42.8812	-10.1845	-2.0367
1.9568	-5.4887	0.2730	11.6849	-1.5092	-4.3956	42.8758	-12.8997	0.2626
1.9592	-4.3026	1.0463	11.7009	-6.9995	-4.0170	42.8783	-10.1738	2.0081
1.9581	-1.5203	1.9565	11.6912	-10.1095	-2.0364	42.8786	-7.0428	4.0162
			11.6980	-12.8241	0.2501			
			11.6980	-10.0943	2.0171			
			11.7028	-6.9721	4.0172			
			11.7002	-1.4990	4.4119			

Table 4. Pressure tap locations for fuselage longitudinal plots

Port Side Strip		
X	Y	Z
0.7918	-2.9458	0.5714
1.9592	-4.3026	1.0463
3.9141	-6.8134	1.0284
5.849	-7.8167	1.5001
7.8085	-9.1345	1.5104
9.7432	-10.1503	1.5064
11.698	-10.0943	2.0171
13.6497	-10.5845	2.0061
15.5793	-10.7623	2.0184
19.4977	-10.7793	1.9863
23.4019	-10.7914	1.9699
38.9907	-10.7804	2.0169
42.8783	-10.1738	2.0081
46.7548	-8.3504	2.0099
50.6764	-5.4239	1.9896
54.5705	-3.2399	0.9924
58.4792	-2.7404	1.0072
62.3617	-2.7199	1.0343
66.2613	-2.7202	1.0569
70.1652	-2.7268	1.0782
74.048	-2.722	1.1092
75.9986	-2.7132	1.1294

Test Section Ceiling

Drive Shaft

83.13
Center of Hub

84.02
Center of
Shaft Tilt

87.00

Rotor Balance

Tunnel C_L,
Center of
Fuselage Tilt

Test Section Floor
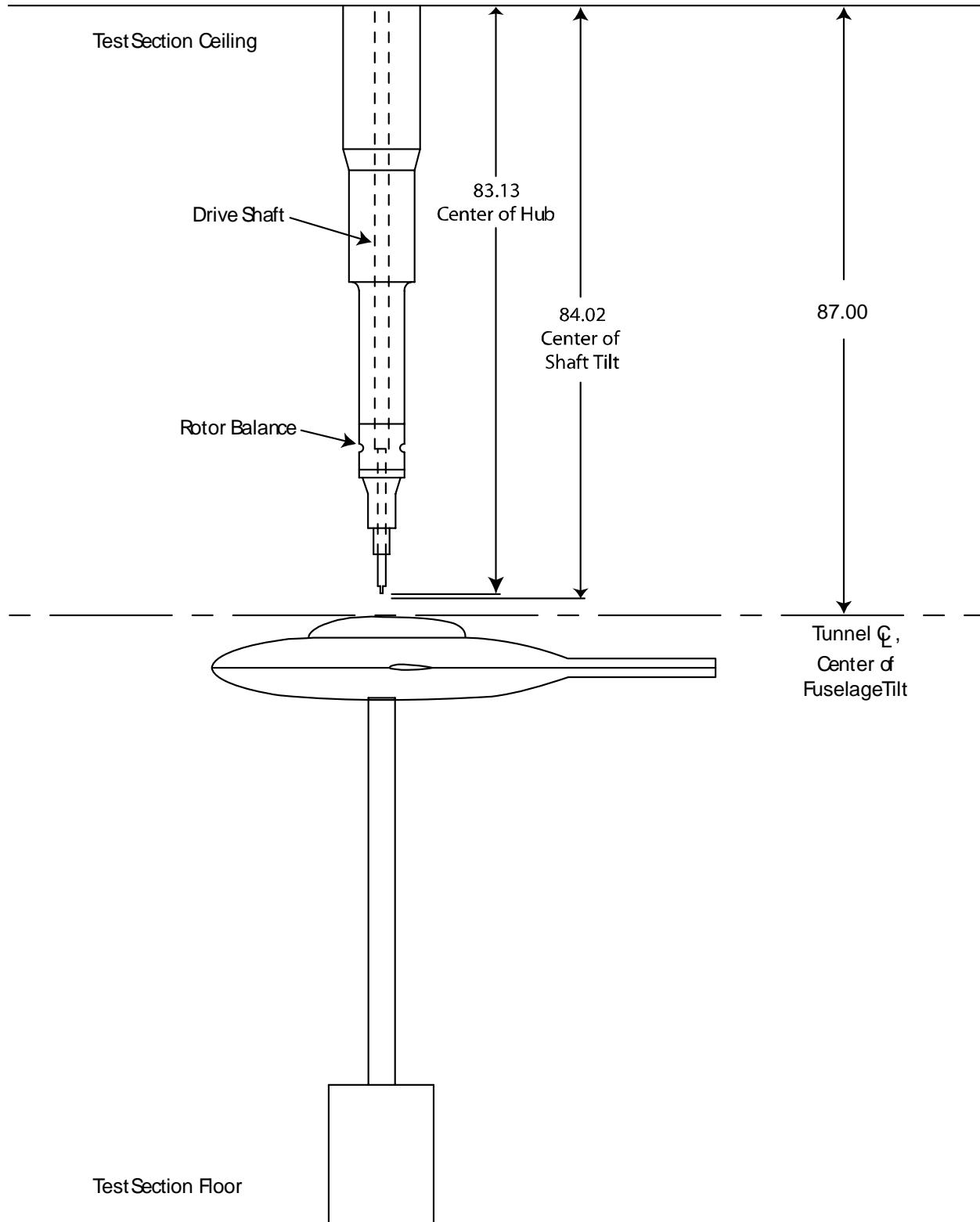
Figure 1. Sketch of the side view of the Isolated Rotor Test System and model arrangement. (All dimensions in inches.)
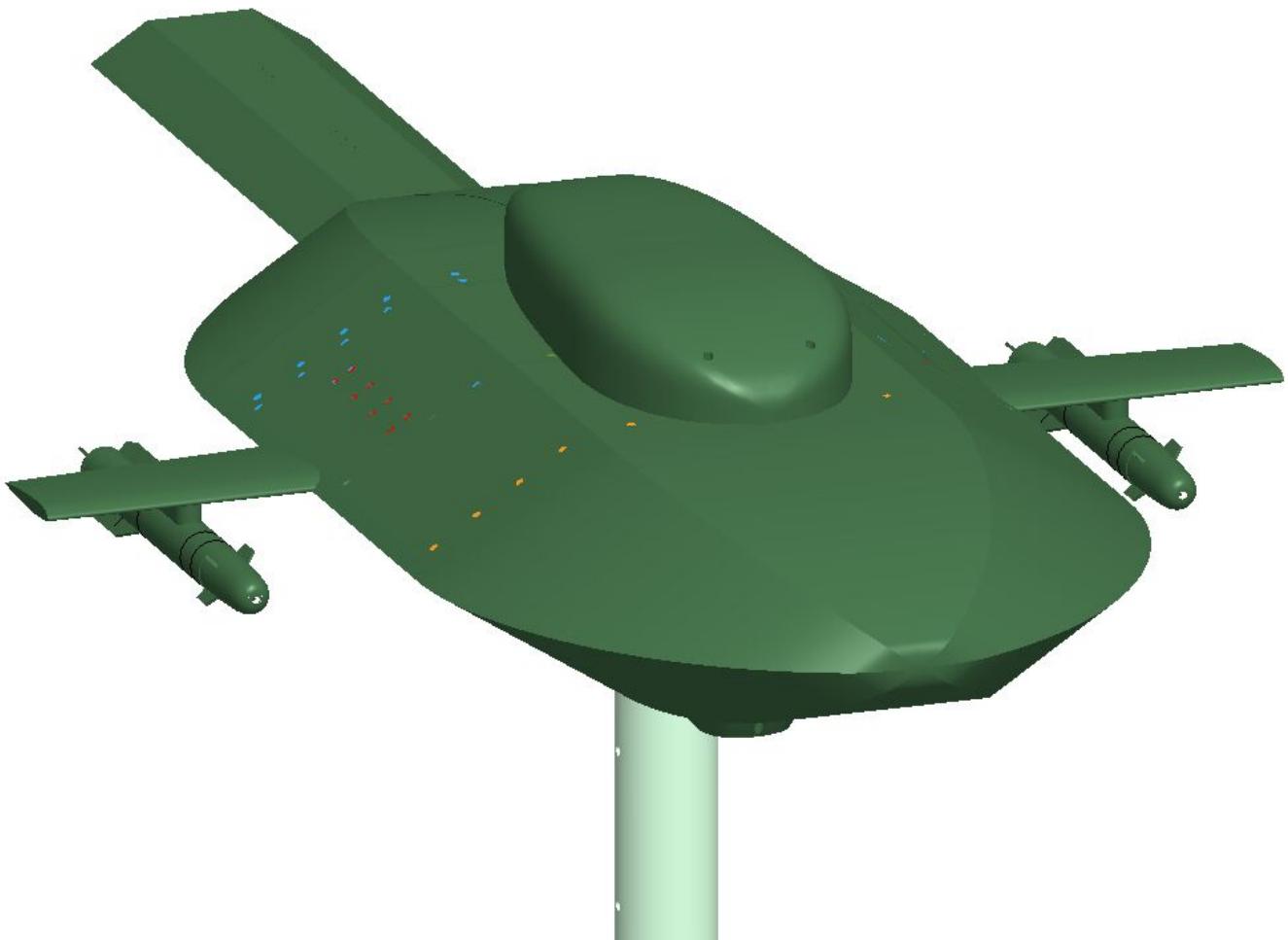
Figure 2. Hex model configuration.
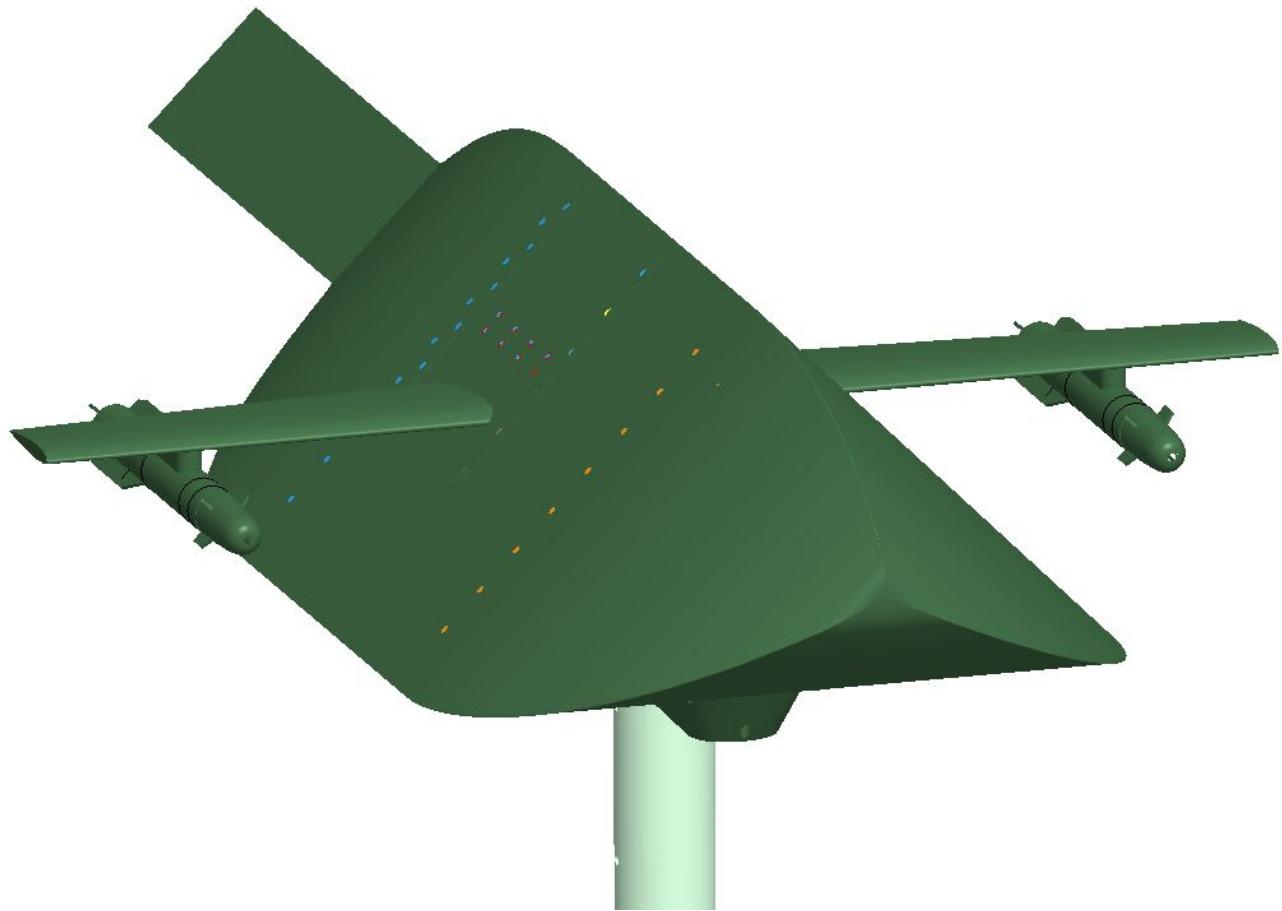
Figure 3. Tri model configuration.
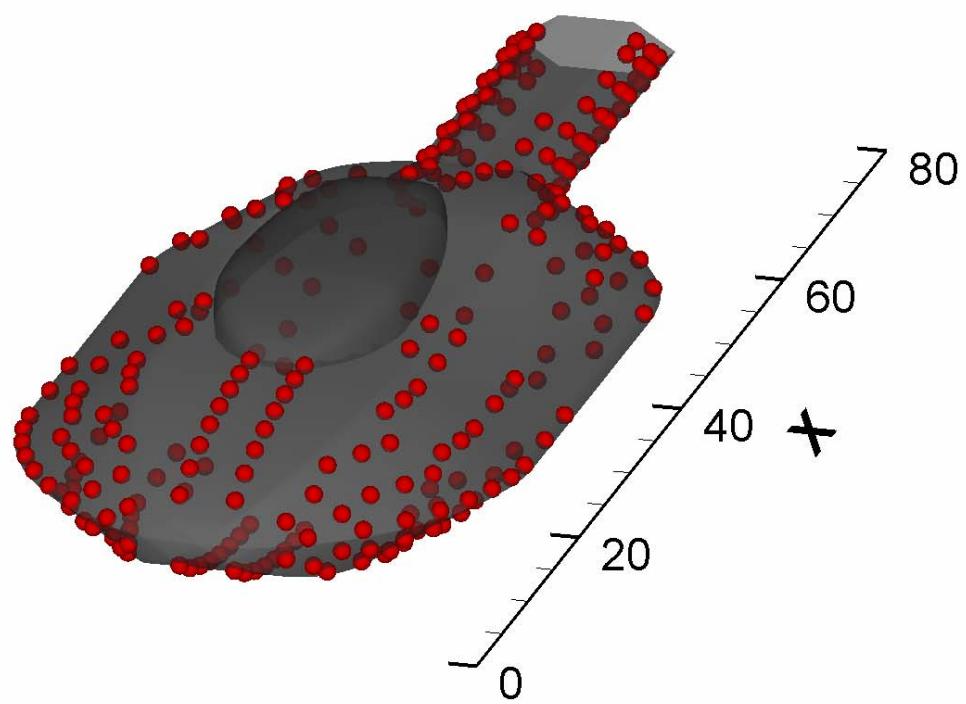
Figure 4. Location of static pressure ports on Hex model.
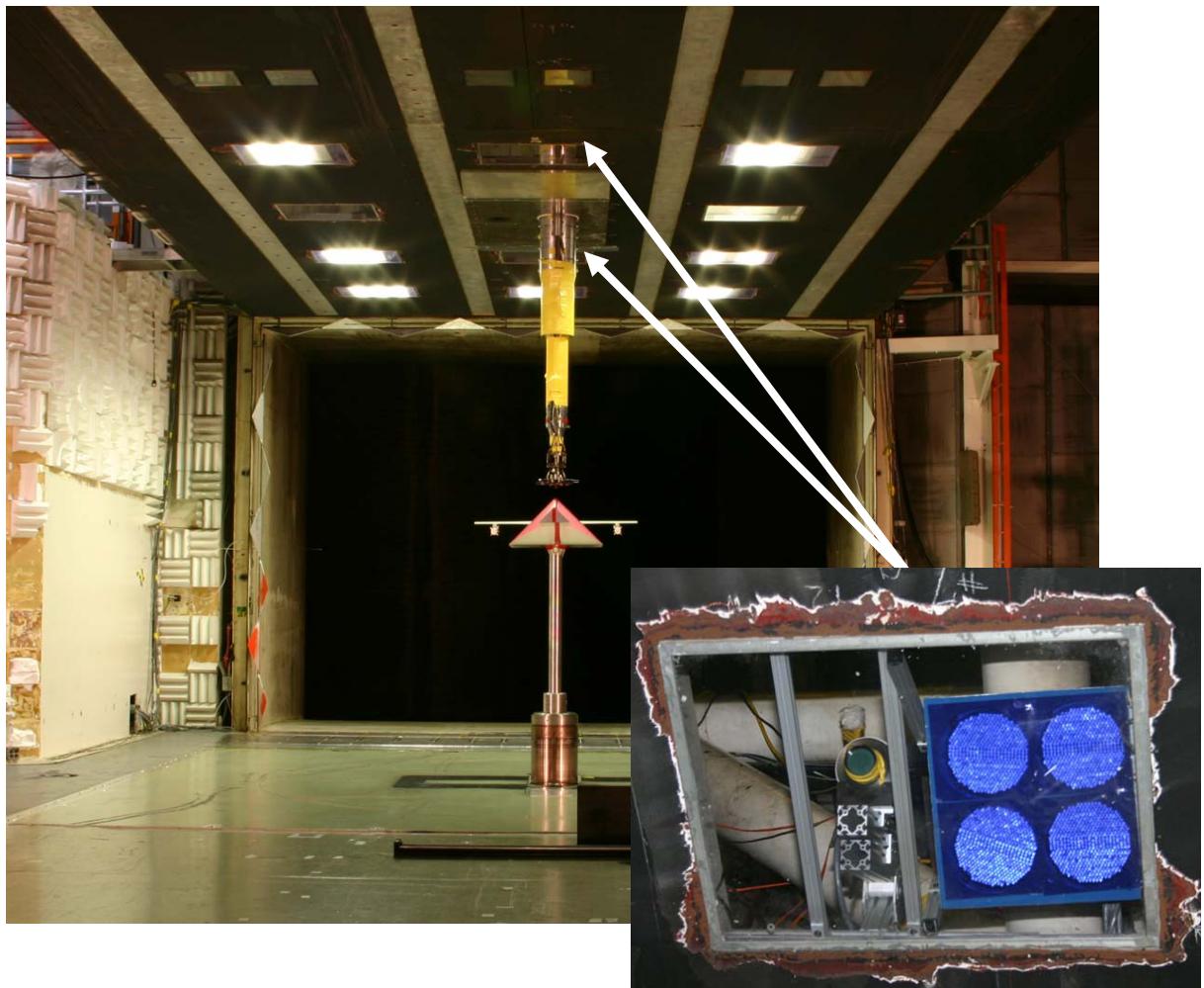
Figure 5. PSP lighting arrangement showing CCD cameras and LED panel placements.
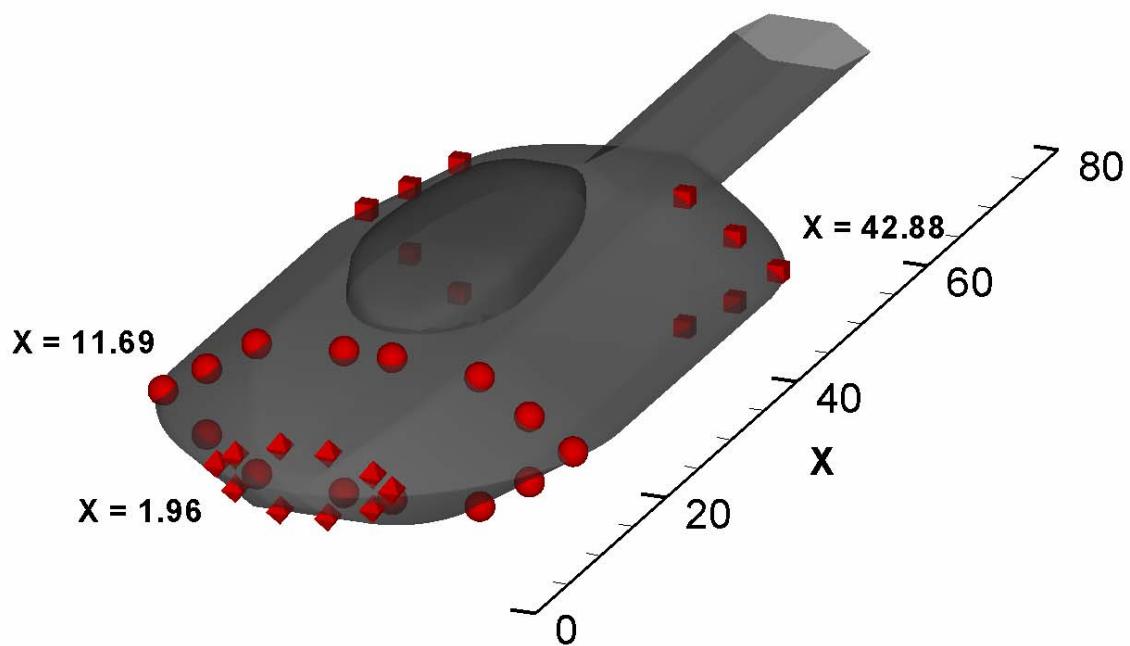
Figure 6. Location of pressure port rows on Hex model selected for presentation of data.
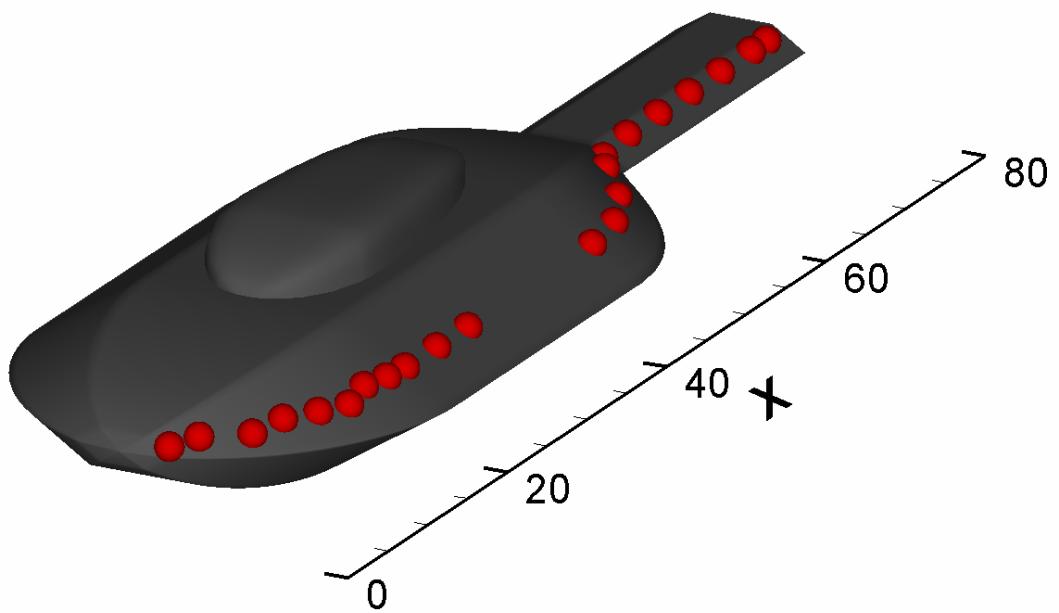
Figure 7. Location of pressure ports along Hex model selected for presentation of data.
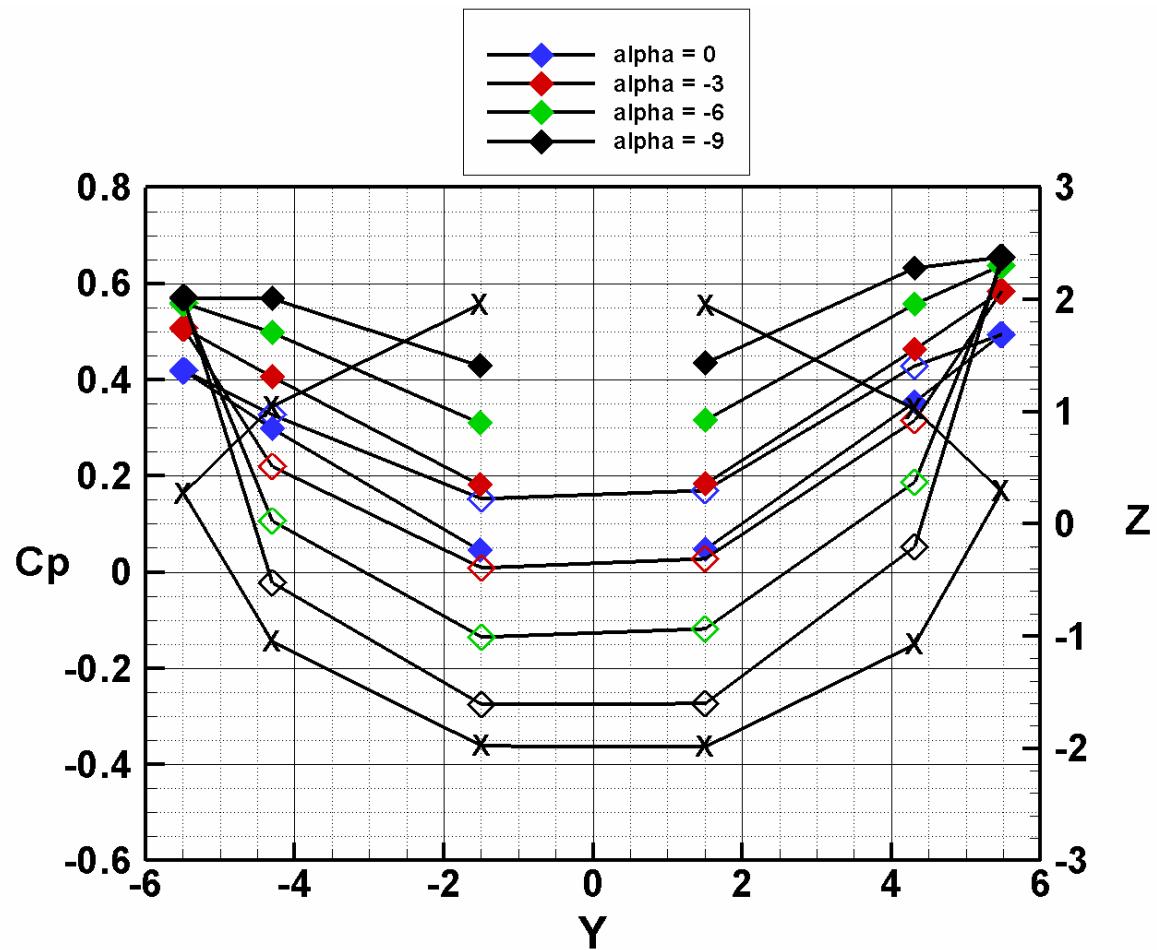
Figure 8. Variation of pressure coefficient with angle-of-attack at station 1.96 of the Hex model, rotor off, β = 0.0, V = 100 KTAS, open symbols are lower surface.
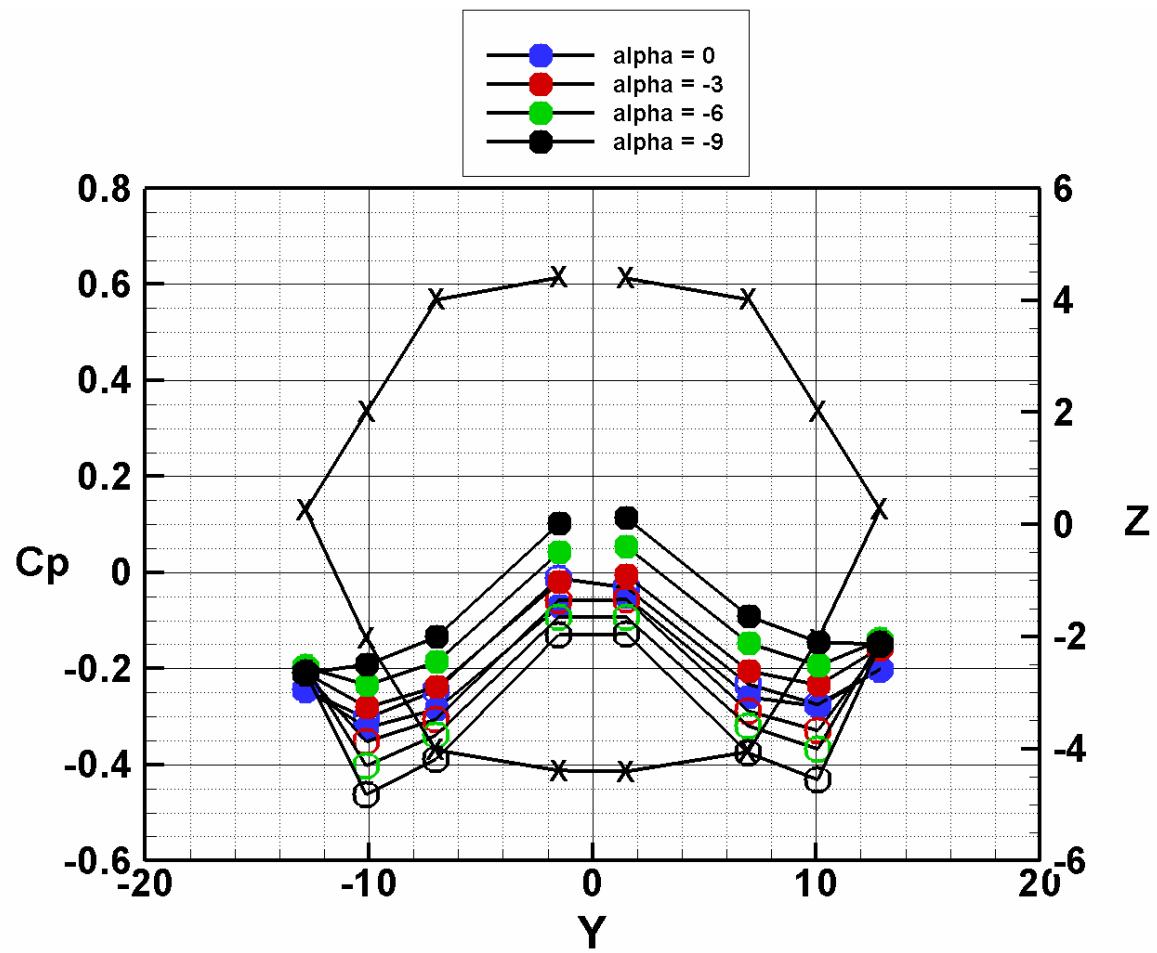
Figure 9. Variation of pressure coefficient with angle-of-attack at station 11.69 of the Hex model, rotor off, β = 0.0, V = 100 KTAS, open symbols are lower surface.
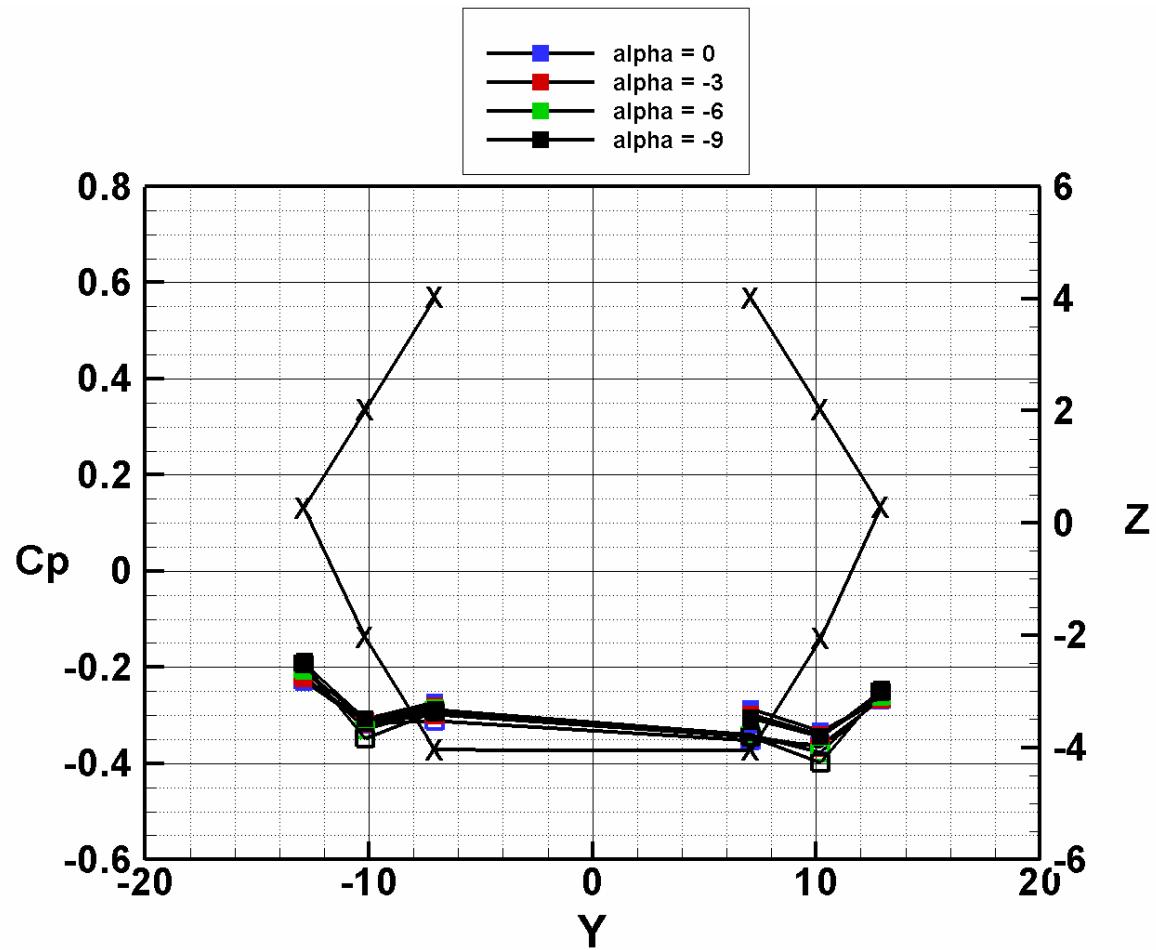
Figure 10. Variation of pressure coefficient with angle-of-attack at station 42.88 of the Hex model,   rotor off, β = 0.0, V = 100 KTAS, open symbols are lower surface.
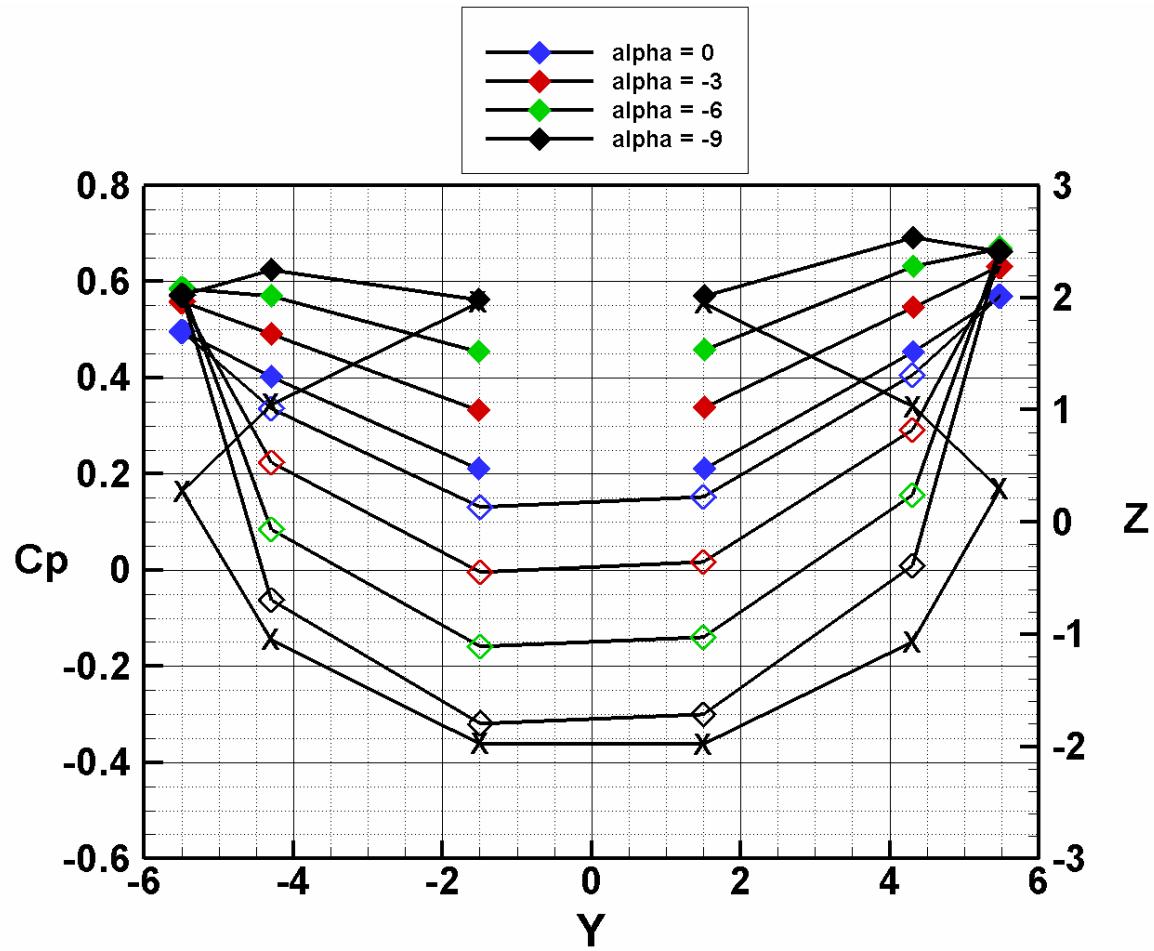
Figure 11. Variation of pressure coefficient with angle-of-attack at station 1.96 of the Hex model, rotor on, β = 0.0, V = 100 KTAS, open symbols are lower surface.
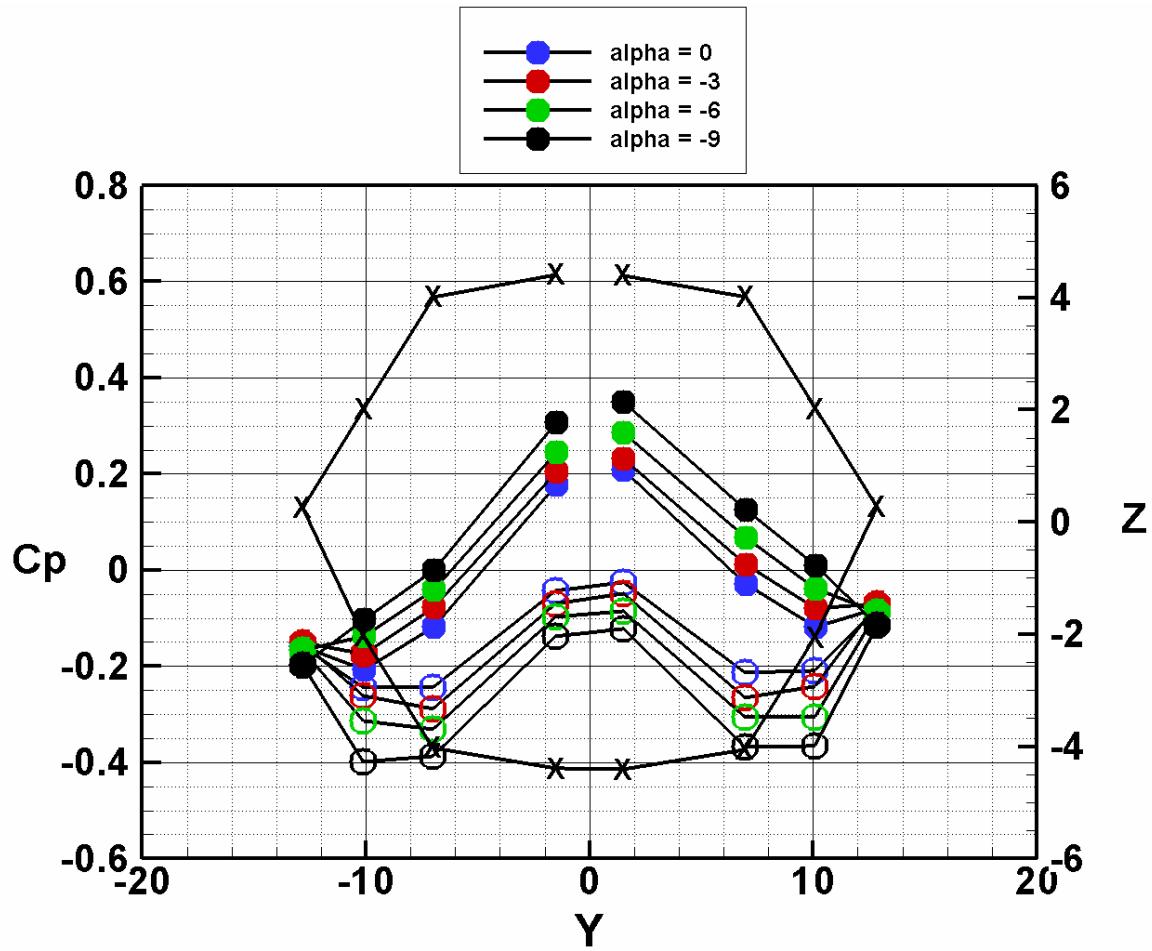
Figure 12. Variation of pressure coefficient with angle-of-attack at station 11.69 of the Hex model, rotor on, β = 0.0, V = 100 KTAS, open symbols are lower surface.
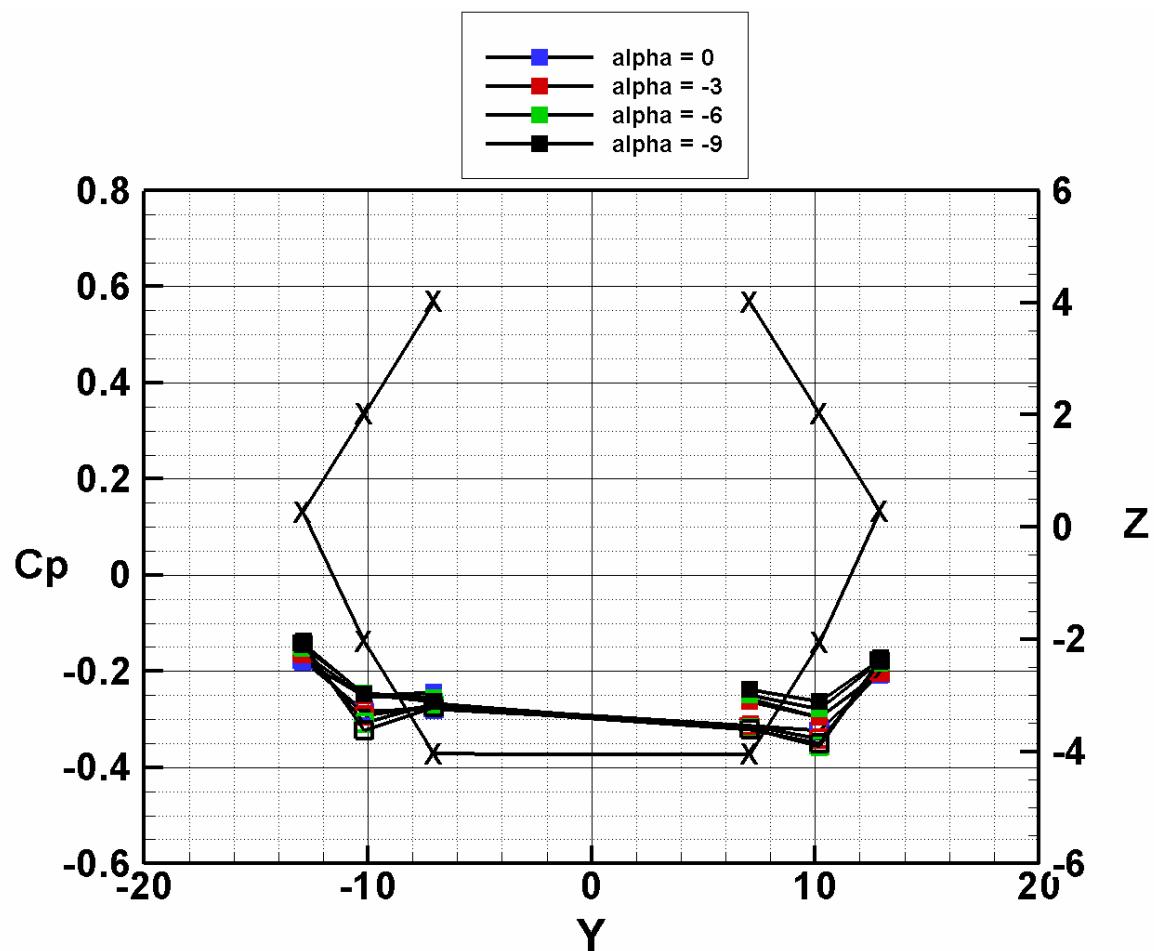
Figure 13. Variation of pressure coefficient with angle-of-attack at station 42.88 of the Hex model, rotor on, β = 0.0, V =100 KTAS, open symbols are lower surface.
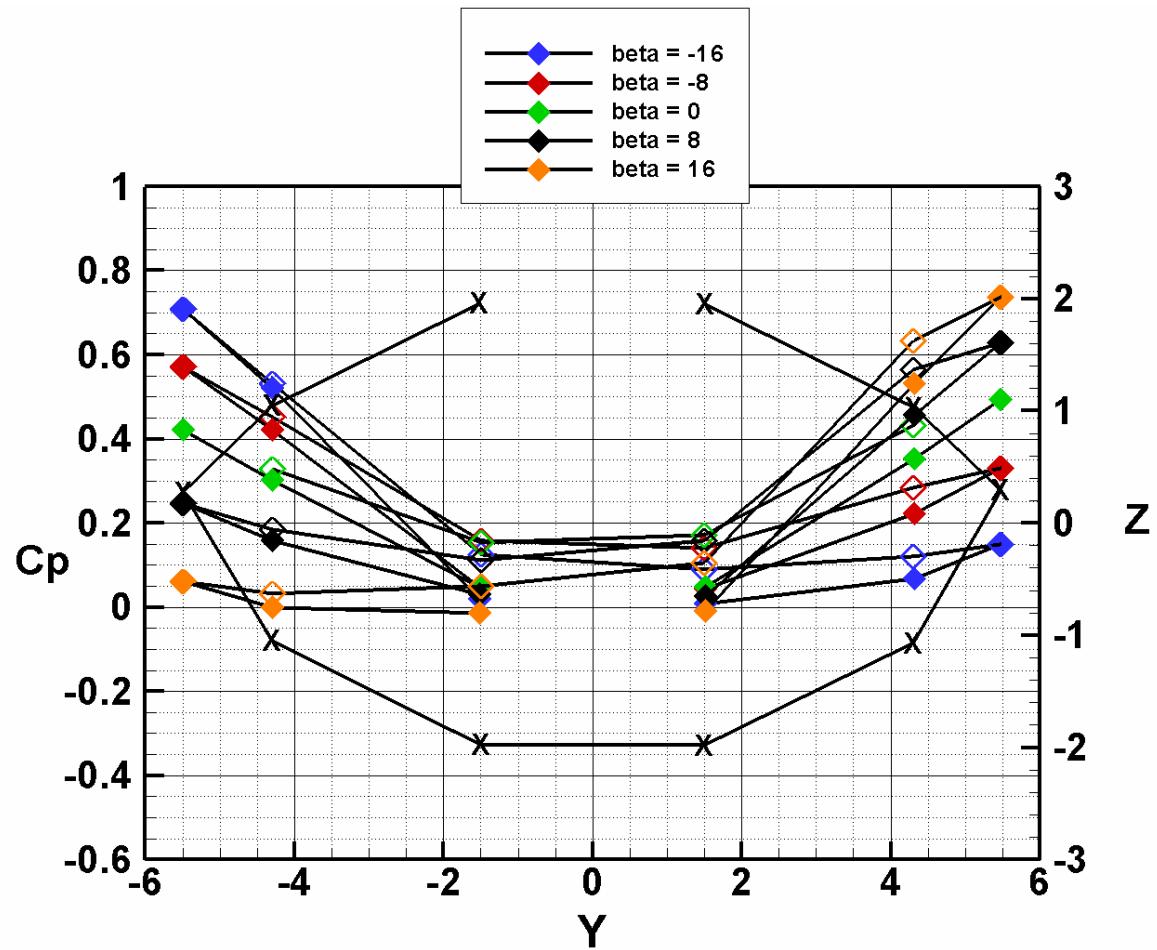
Figure 14. Variation of pressure coefficient with yaw angle at station 1.96 of the Hex model, rotor off, $\alpha = 0.0$, V = 100 KTAS, open symbols are lower surface.
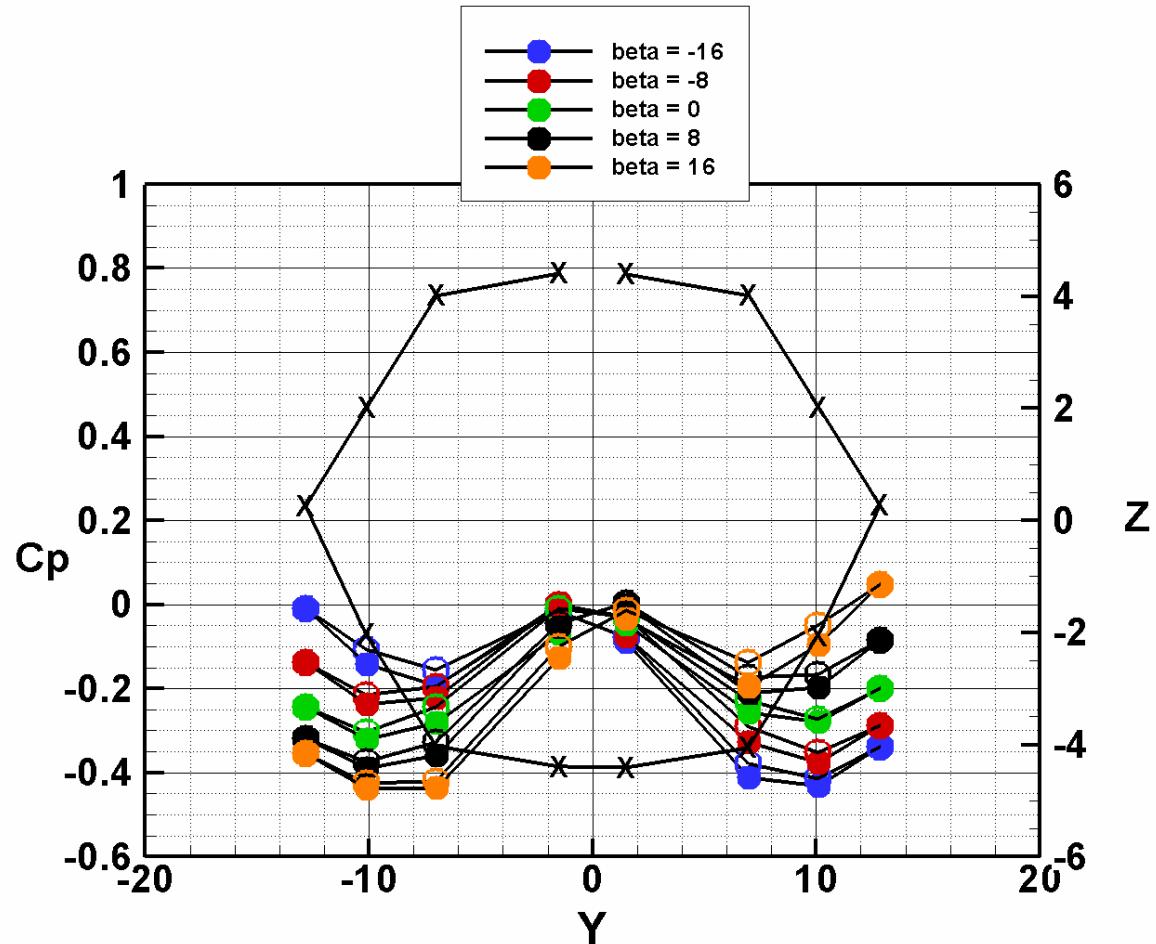
Figure 15. Variation of pressure coefficient with yaw angle at station 11.69 of the Hex model, rotor off, α = 0.0, V = 100 KTAS, open symbols are lower surface.
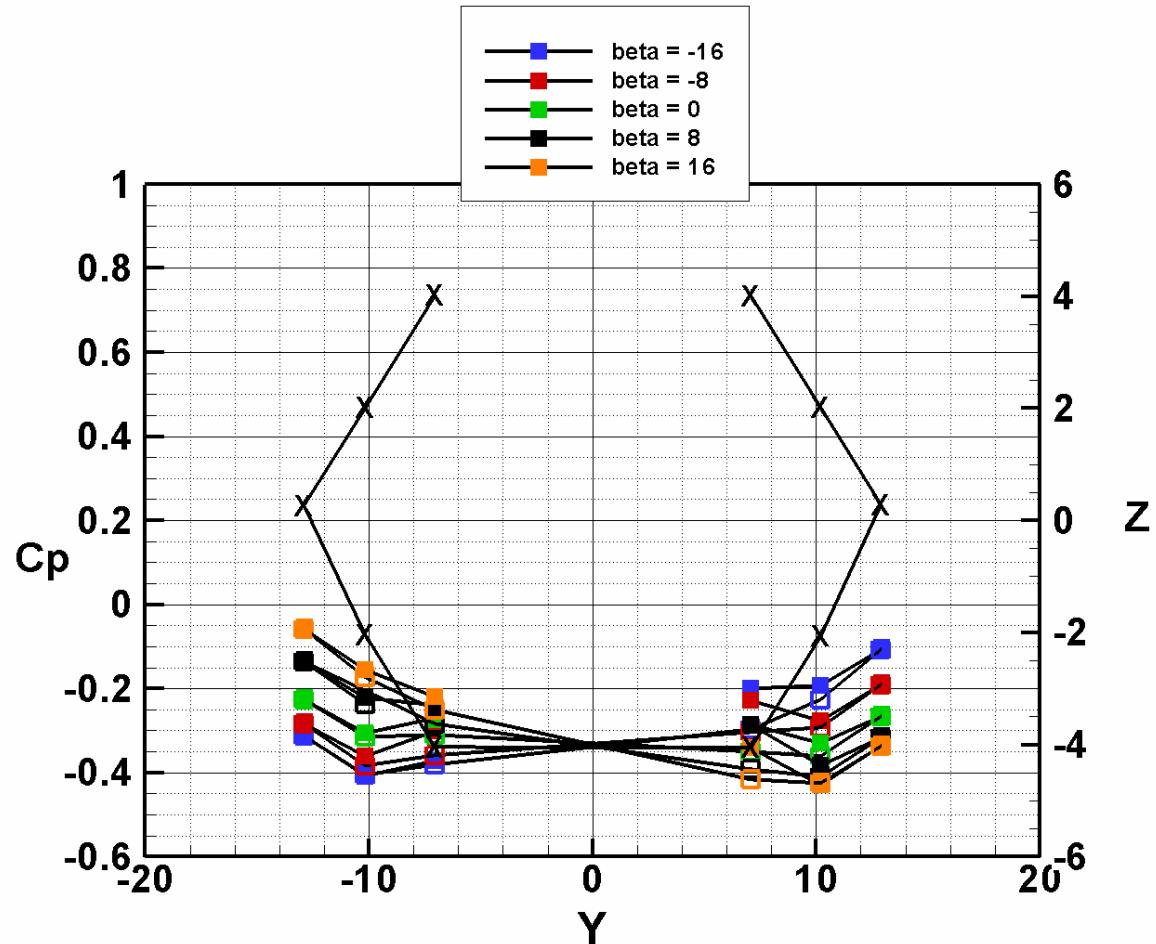
Figure 16. Variation of pressure coefficient with yaw angle at station 42.88 of the Hex model, rotor off, $\alpha = 0.0$, V = 100 KTAS, open symbols are lower surface.
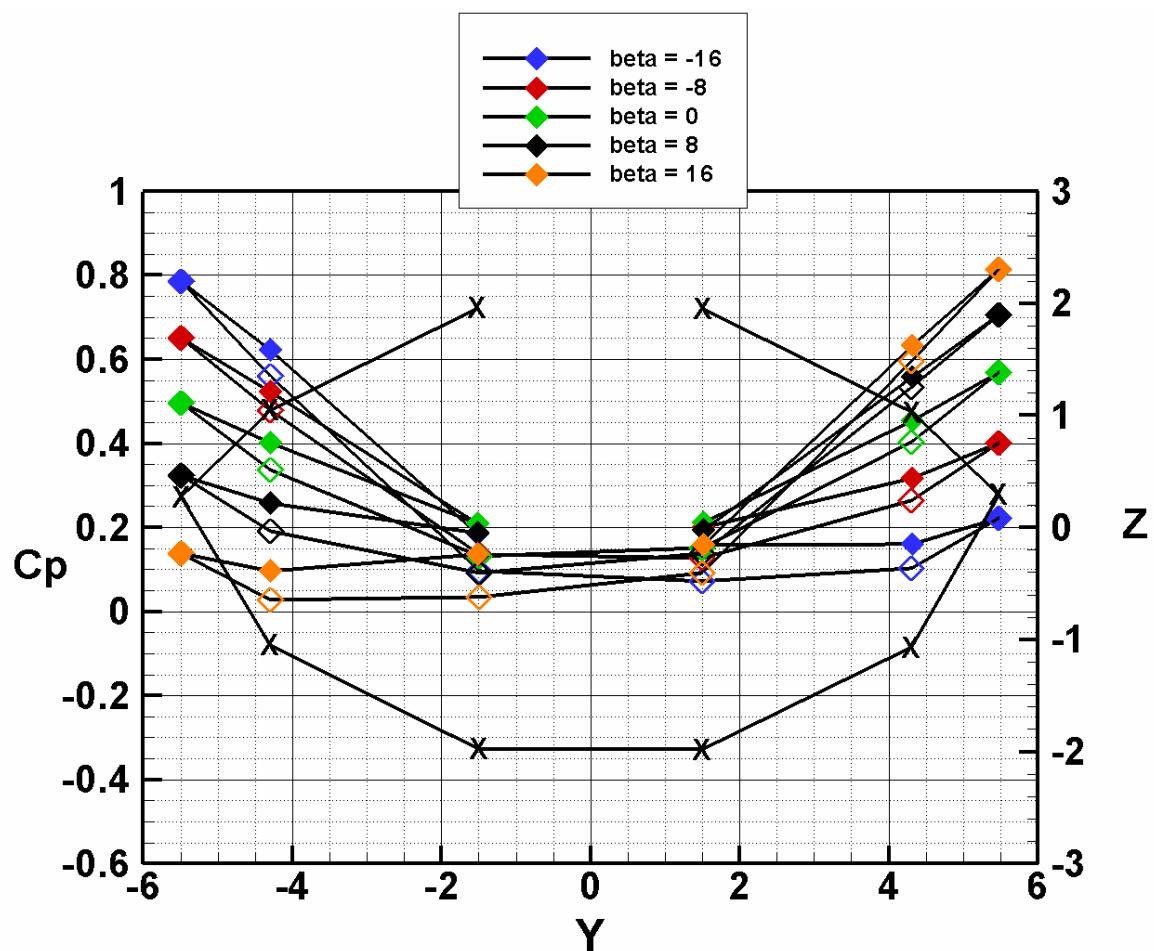
Figure 17. Variation of pressure coefficient with yaw angle at station 1.96 of the Hex model, rotor on, $\alpha = 0.0$, V = 100 KTAS, open symbols are lower surface.
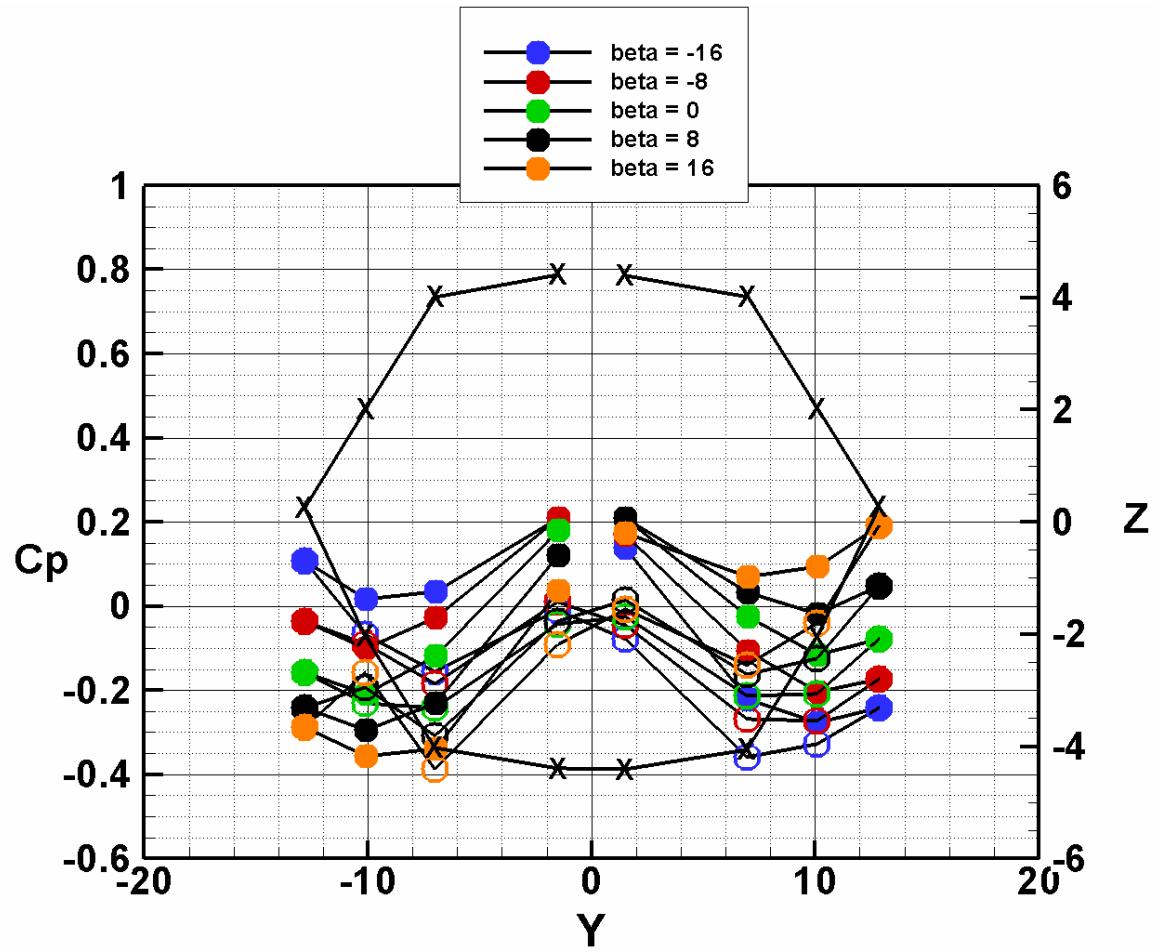
Figure 18. Variation of pressure coefficient with yaw angle at station 11.69 of the Hex model, rotor on, $\alpha = 0.0$, V = 100 KTAS, open symbols are lower surface.
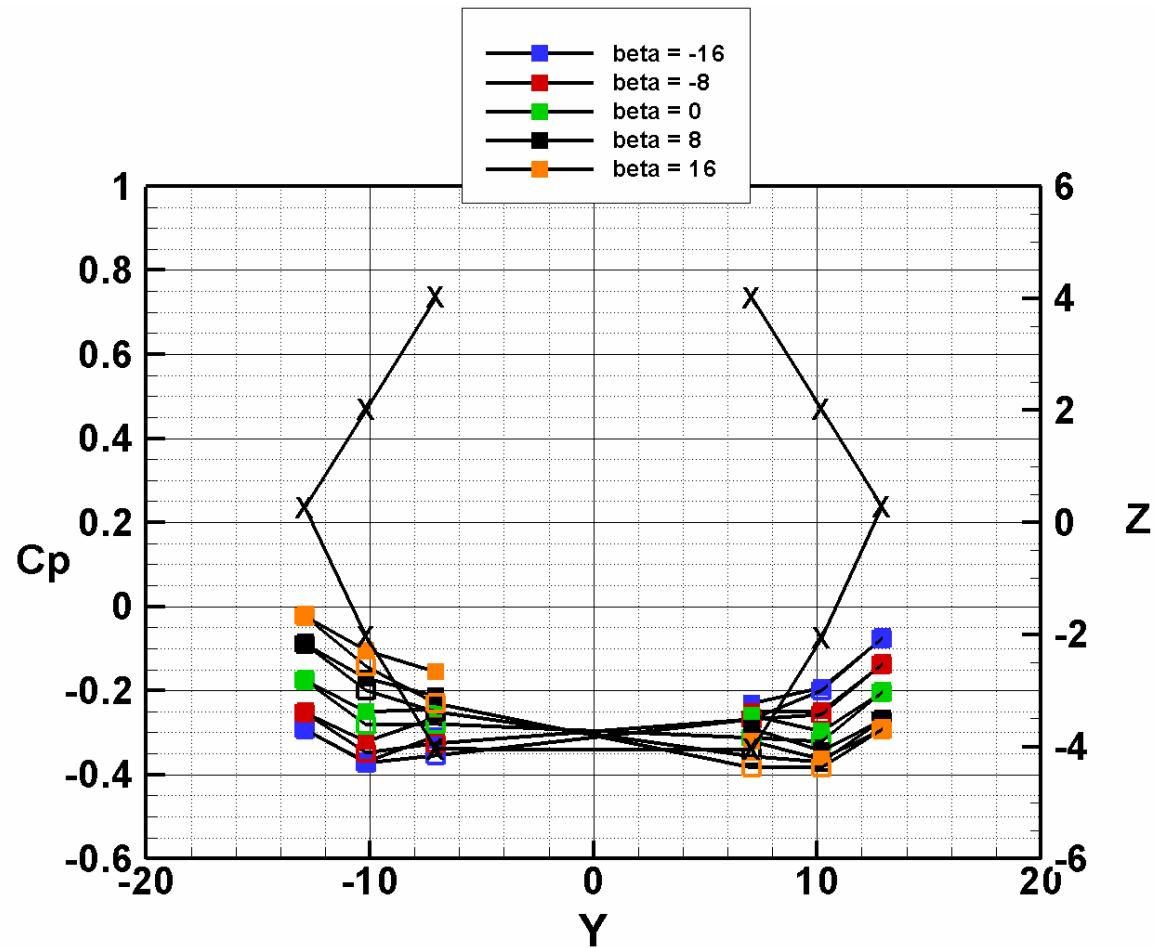
Figure 19. Variation of pressure coefficient with yaw angle at station 42.88 of the Hex model, rotor on, $\alpha = 0.0$, V = 100 KTAS, open symbols are lower surface.
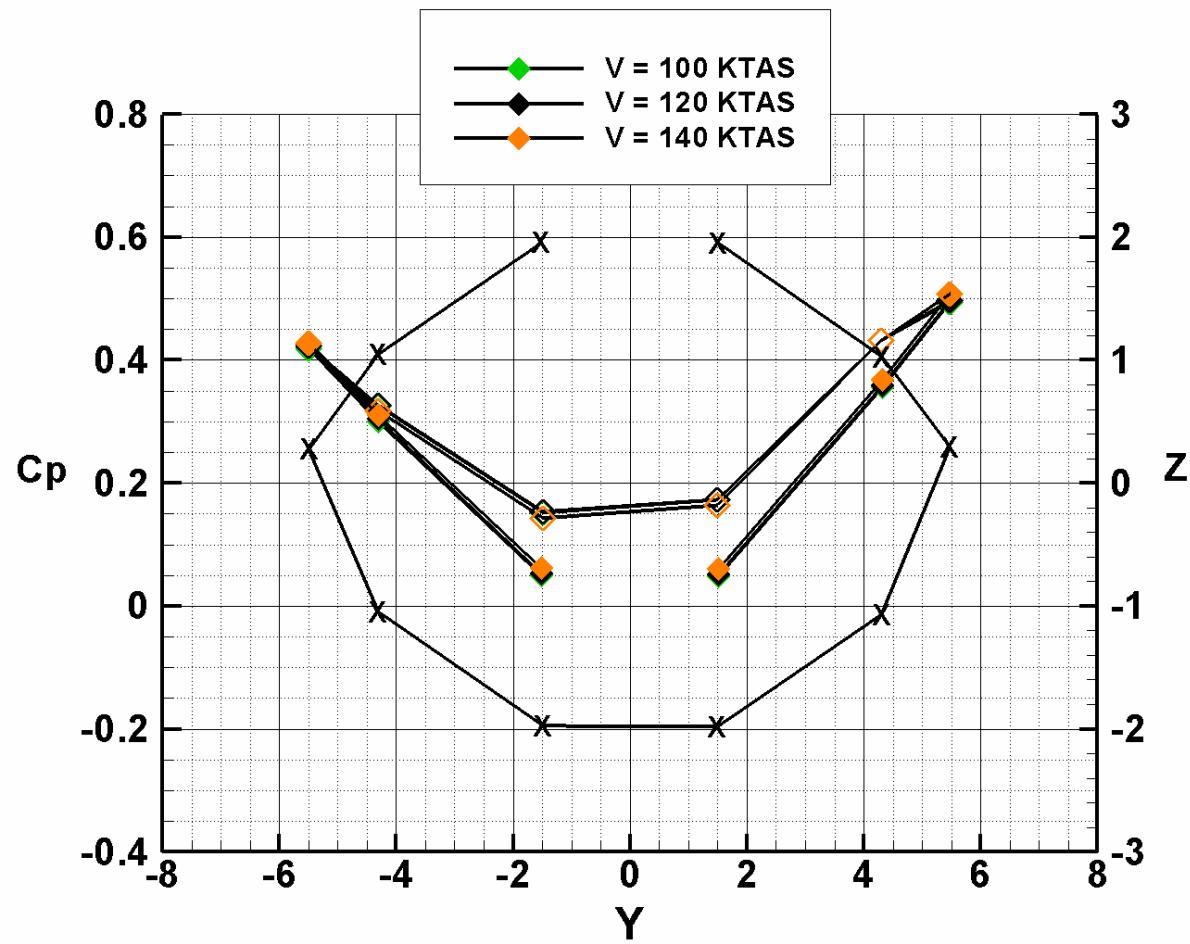
Figure 20. Variation of pressure coefficient with speed at station 1.96 of the Hex model, rotor off, $\alpha = \beta = 0.0$, open symbols are lower surface.
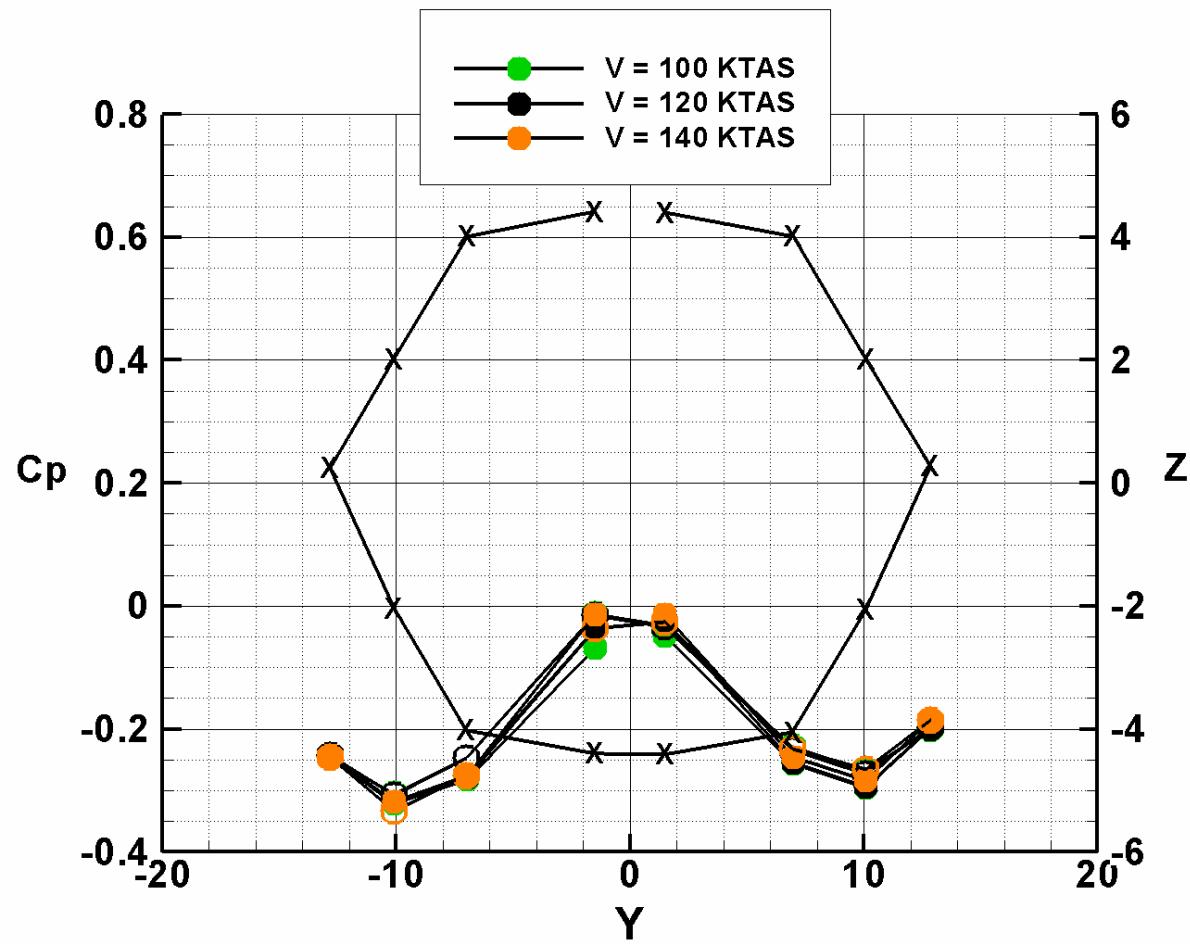
Figure 21. Variation of pressure coefficient with speed at station 11.69 of the Hex model, rotor off, α = β= 0.0, open symbols are lower surface.
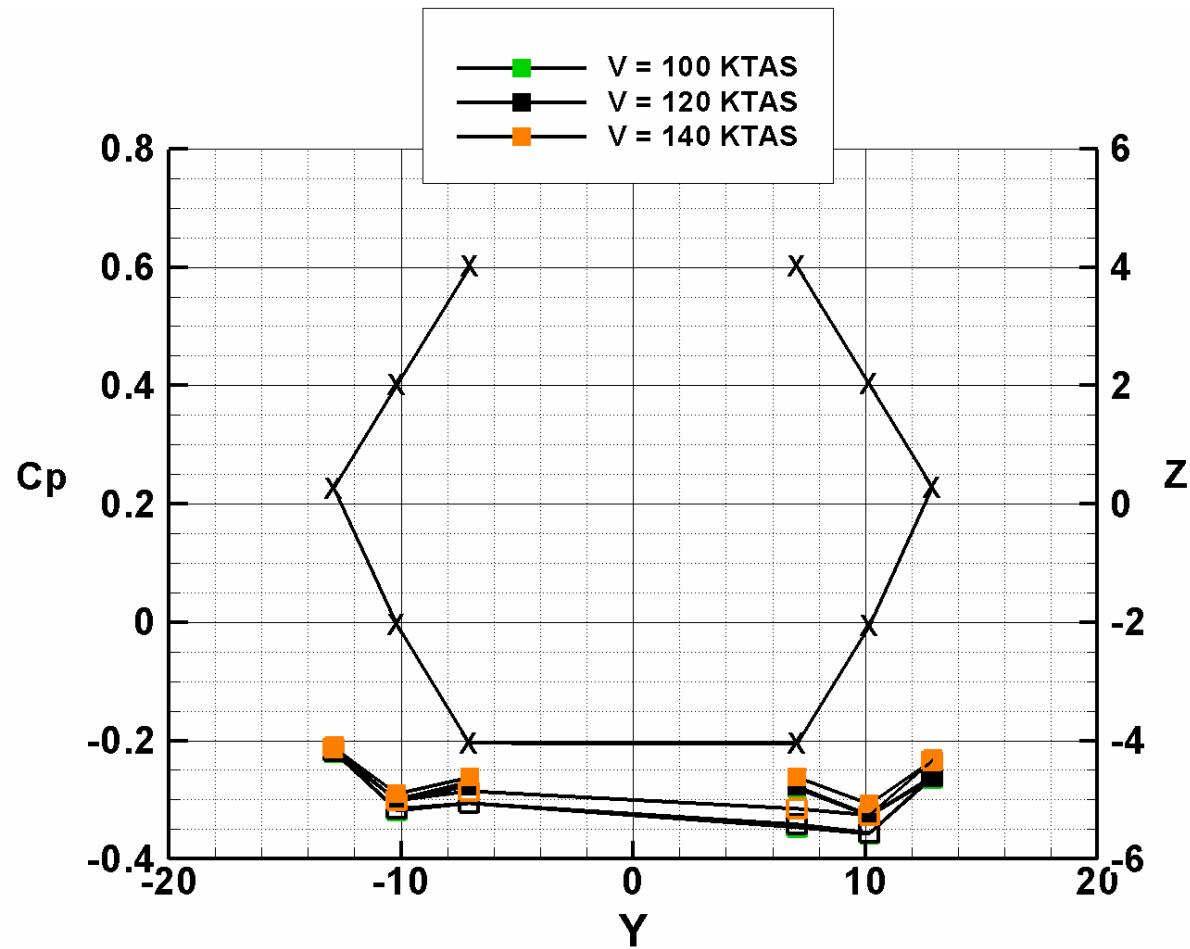
Figure 22. Variation of pressure coefficient with speed at station 42.88 of the Hex model, rotor off, α = β = 0.0, open symbols are lower surface.
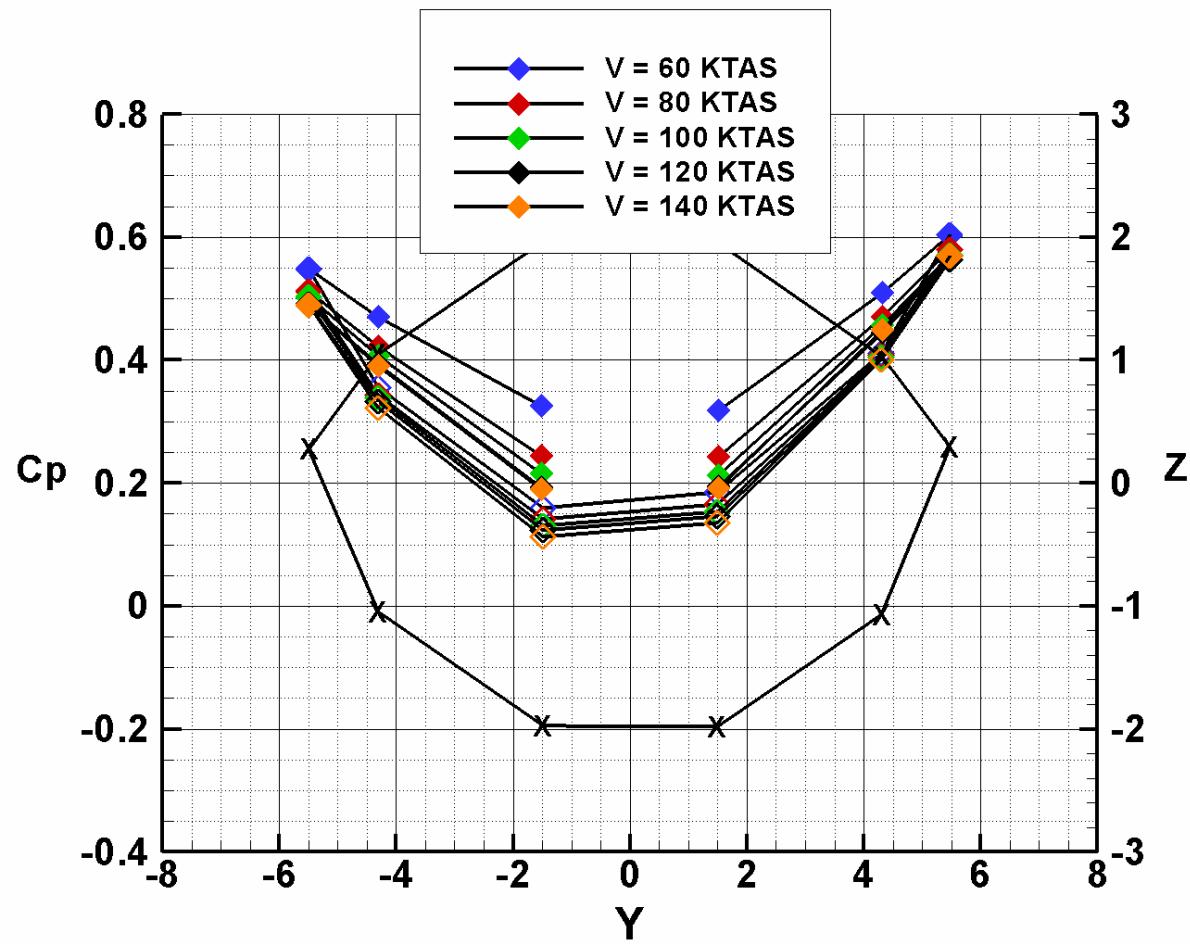
Figure 23. Variation of pressure coefficient with speed at station 1.96 of the Hex model, rotor on, $\alpha = \beta = 0.0$, open symbols are lower surface.
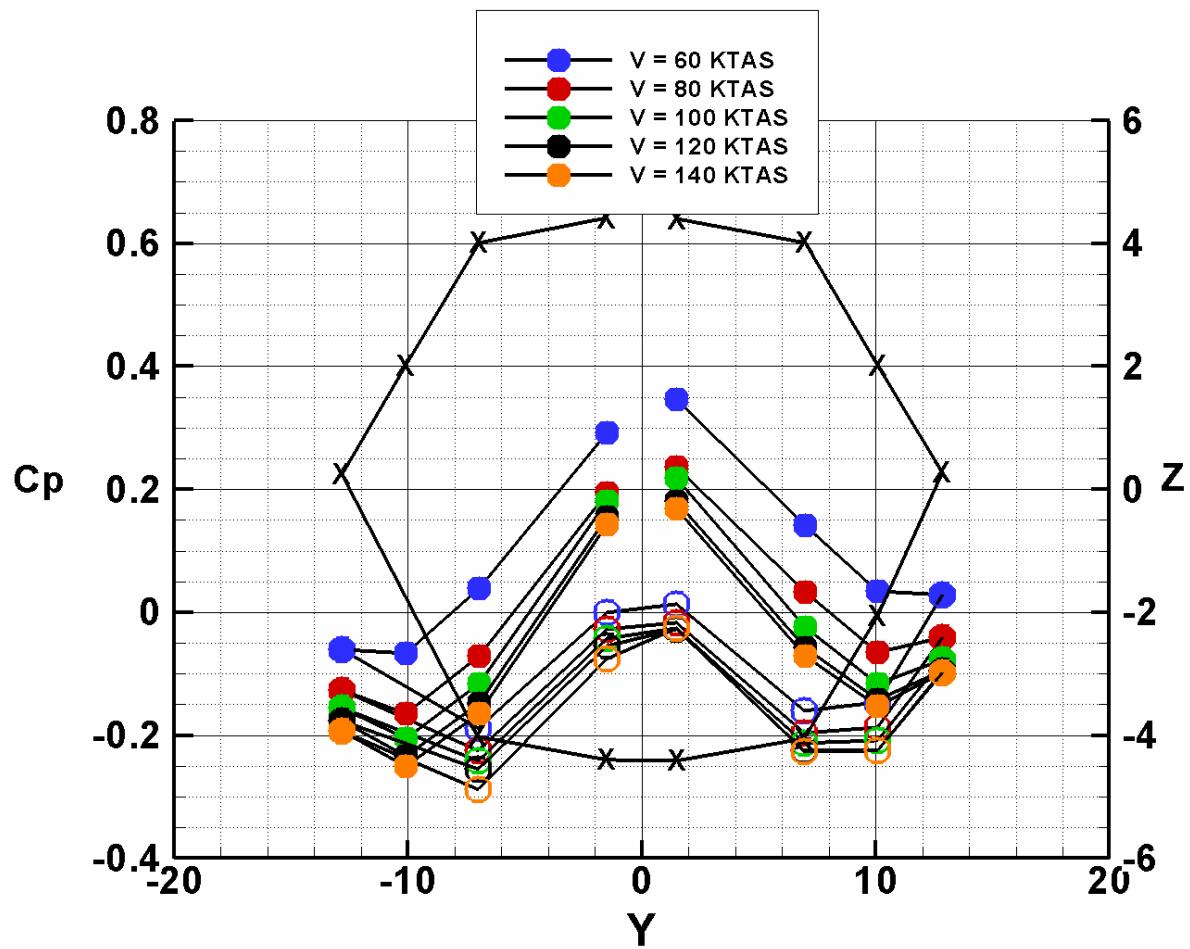
Figure 24. Variation of pressure coefficient with speed at station 11.69 of the Hex model, rotor on, α = β= 0.0, open symbols are lower surface.
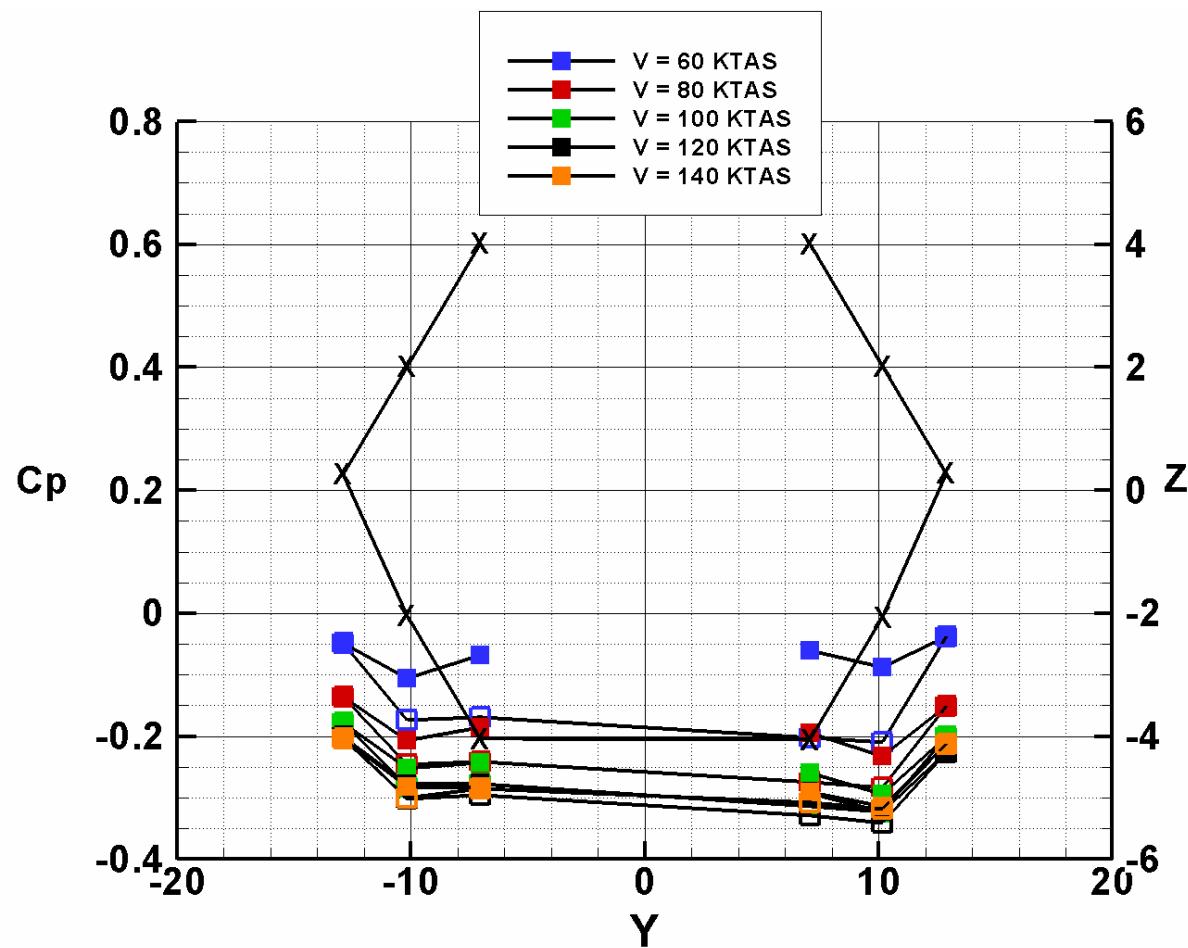
Figure 25. Variation of pressure coefficient with speed at station 42.88 of the Hex model, rotor on, $\alpha = \beta = 0.0$, open symbols are lower surface.
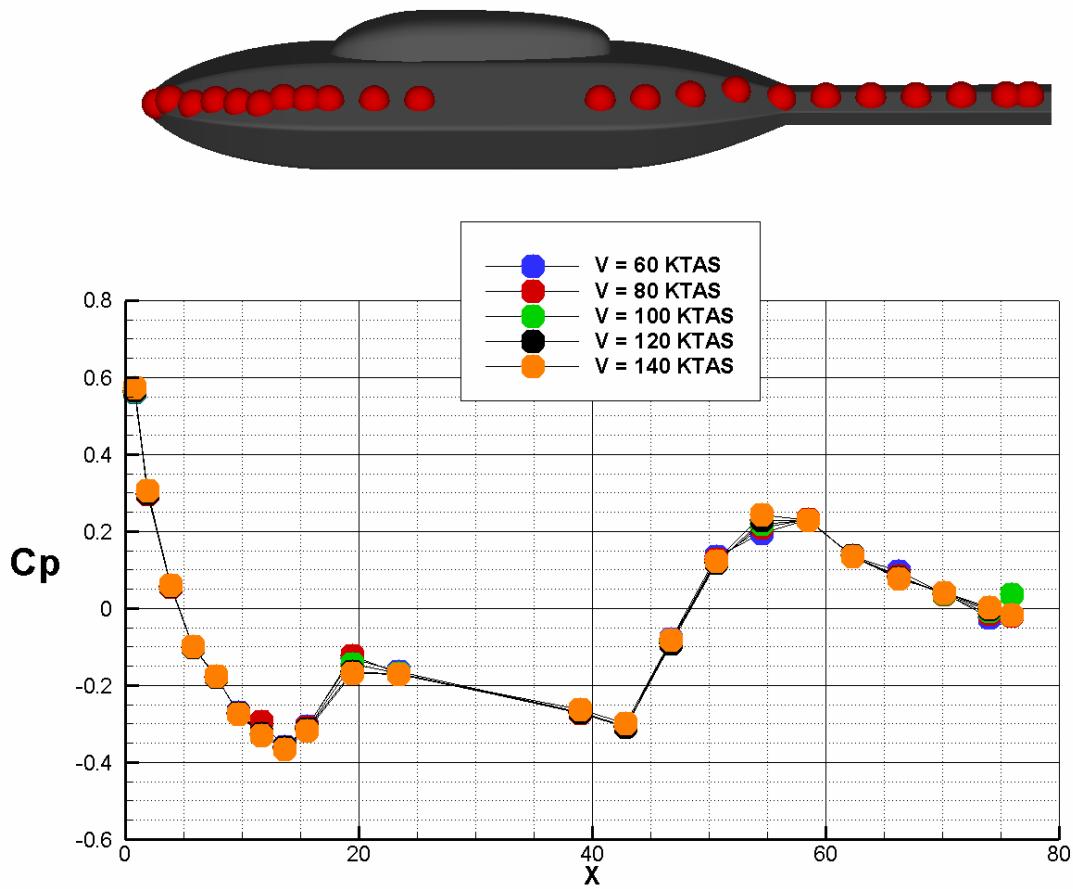
Figure 26. Variation of pressure coefficient along the upper surface of the Hex model (body+wing) with speed, no rotor, $\alpha = \beta = 0.0$.
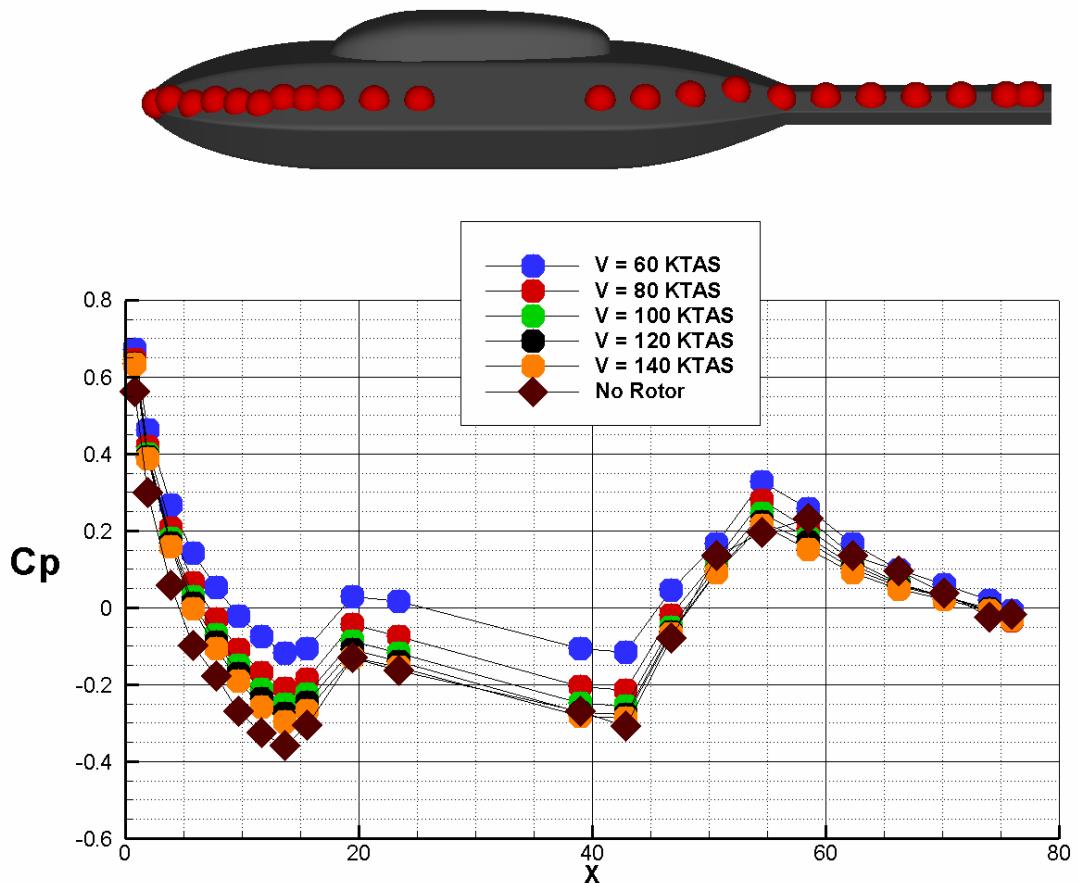
Figure 27. Variation of pressure coefficient along the upper surface of the Hex model (body+ wing) with speed with and without the rotor, $\alpha = \beta = 0.0$.
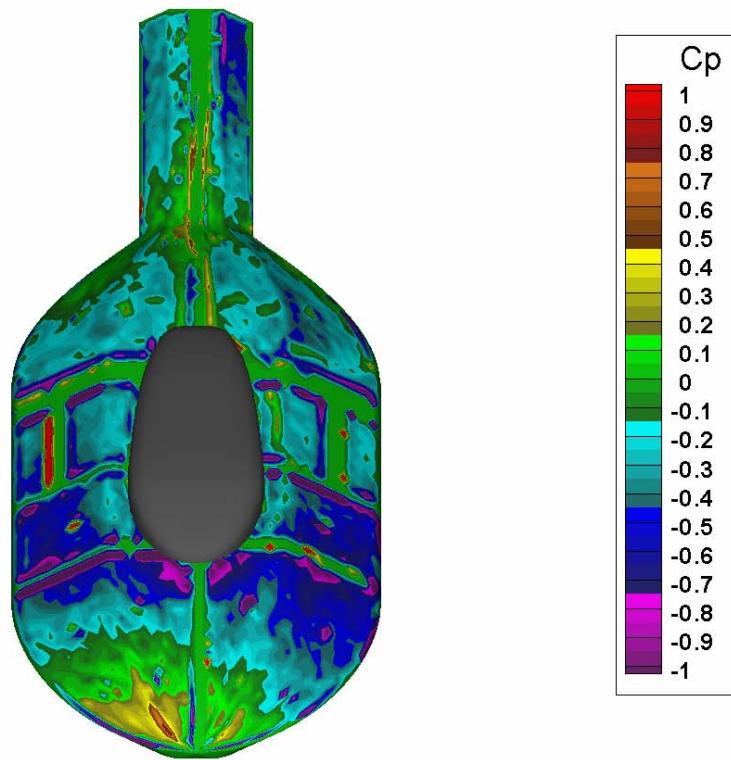
Figure 28. PSP measured pressure coefficient contour on the Hex model basic body, no rotor, α=β= 0.0, speed is 100 KTAS.
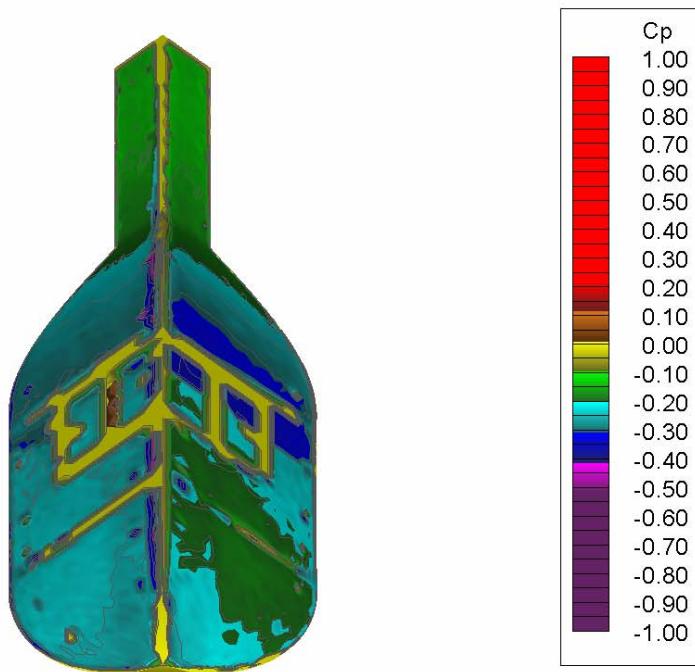
Figure 29. PSP measured pressure coefficient contour on the Tri model basic body, no rotor, α=β= 0.0, speed is 100 KTAS.
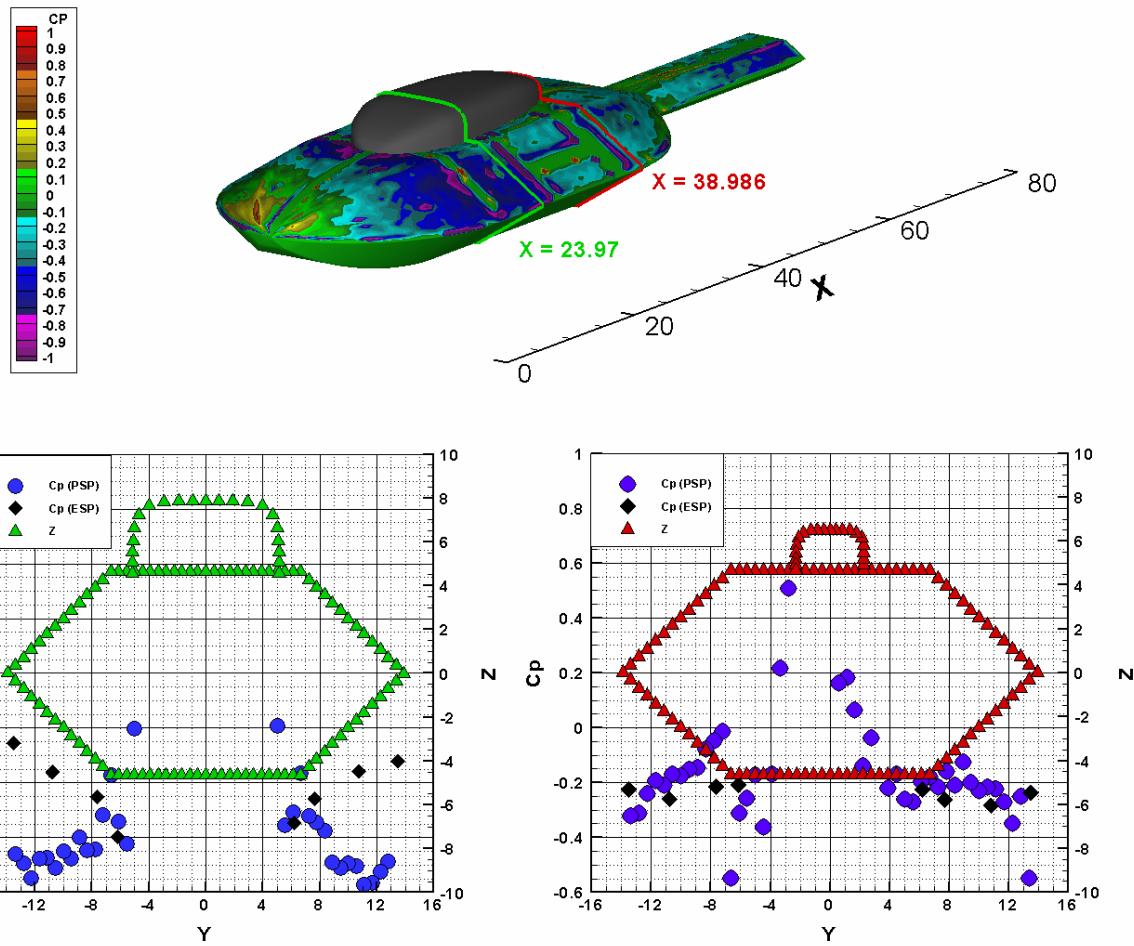
Figure 30. Comparison of PSP and ESP measured Pressure coefficient contour at two stations on the Hex model basic body, no rotor, at $\alpha = 0.0$.
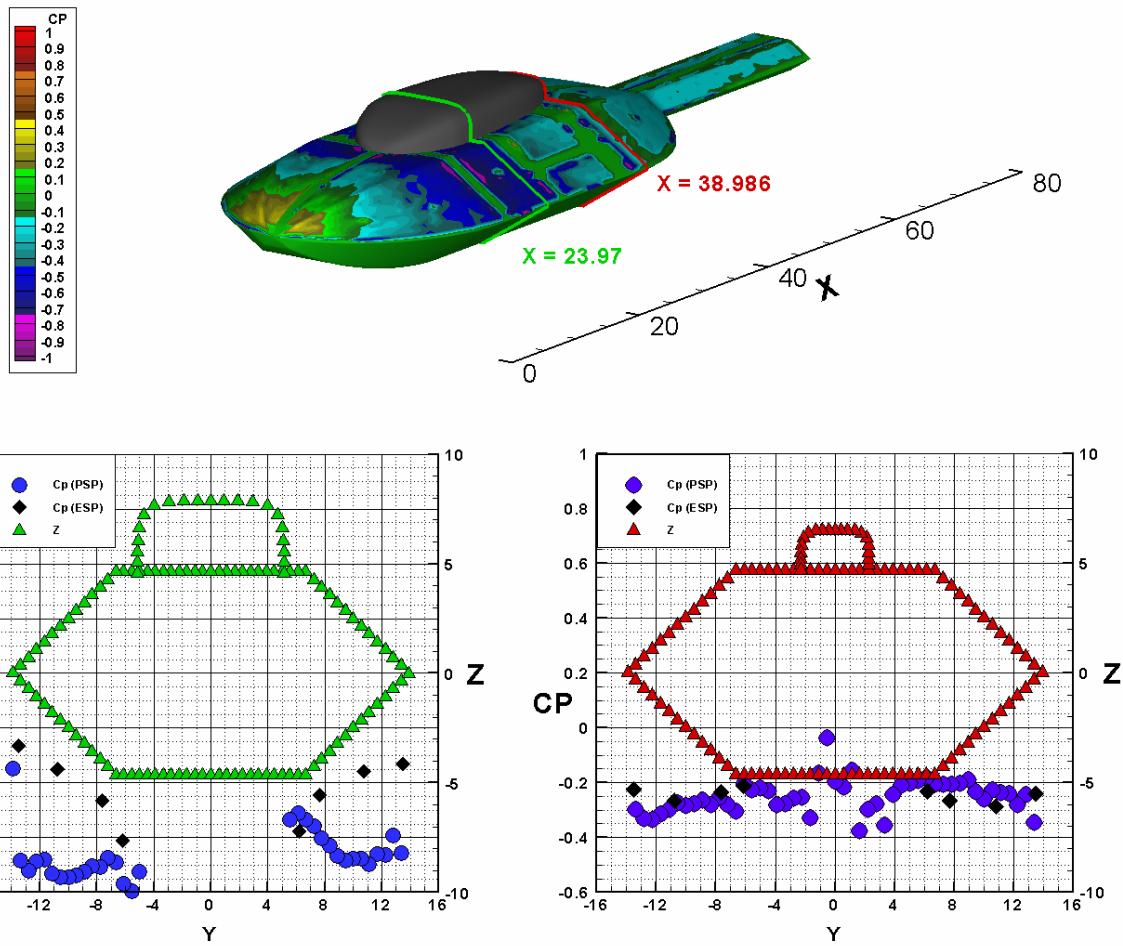
Figure 31. Comparison of PSP and ESP measured pressure coefficient contour at two stations on the Hex model basic body, no rotor, at $\alpha = -2.65$
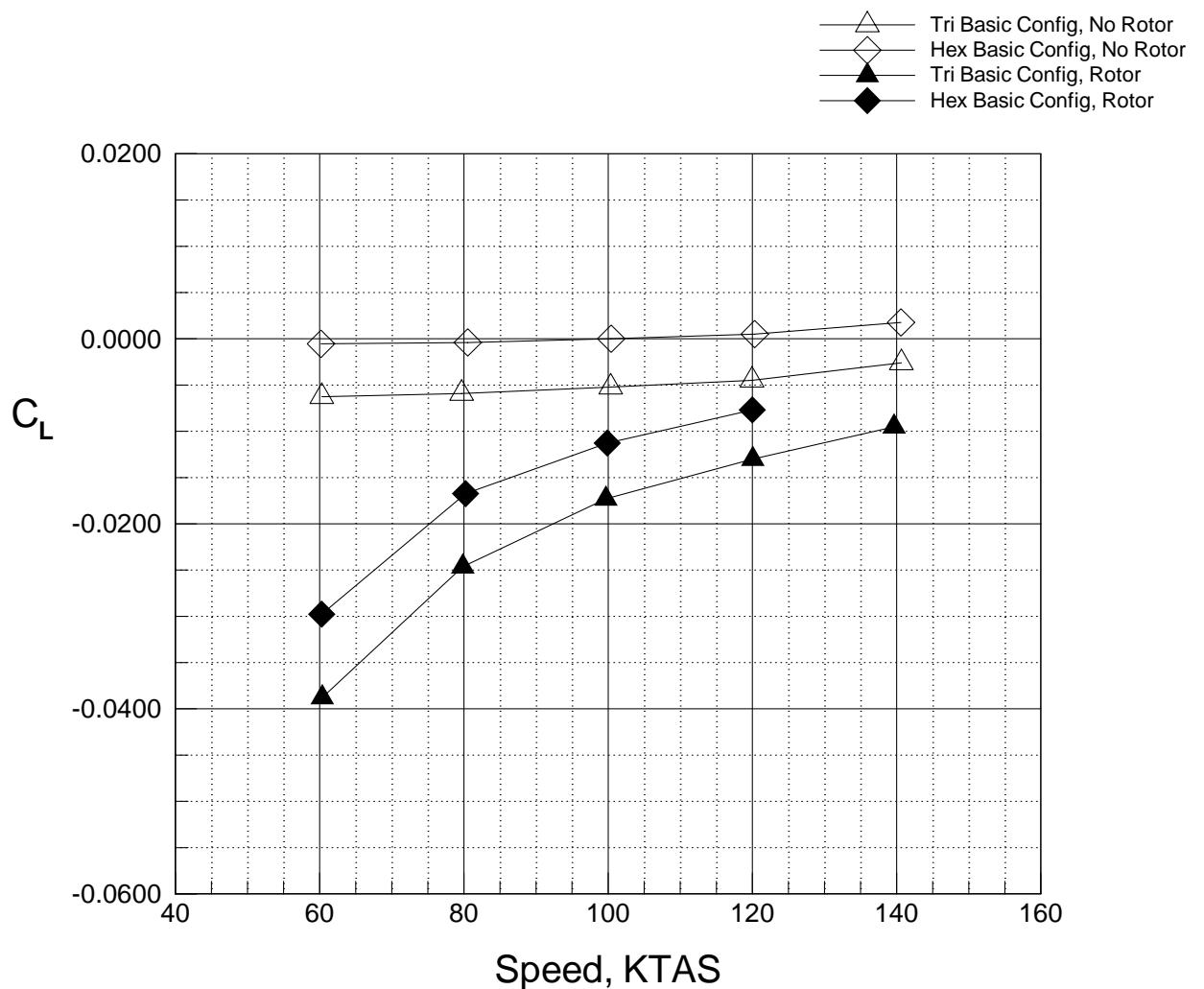
Fig 32. Variation of lift coefficient with speed for both basic configurations with and without the rotor,
$\alpha = \beta = 0.$
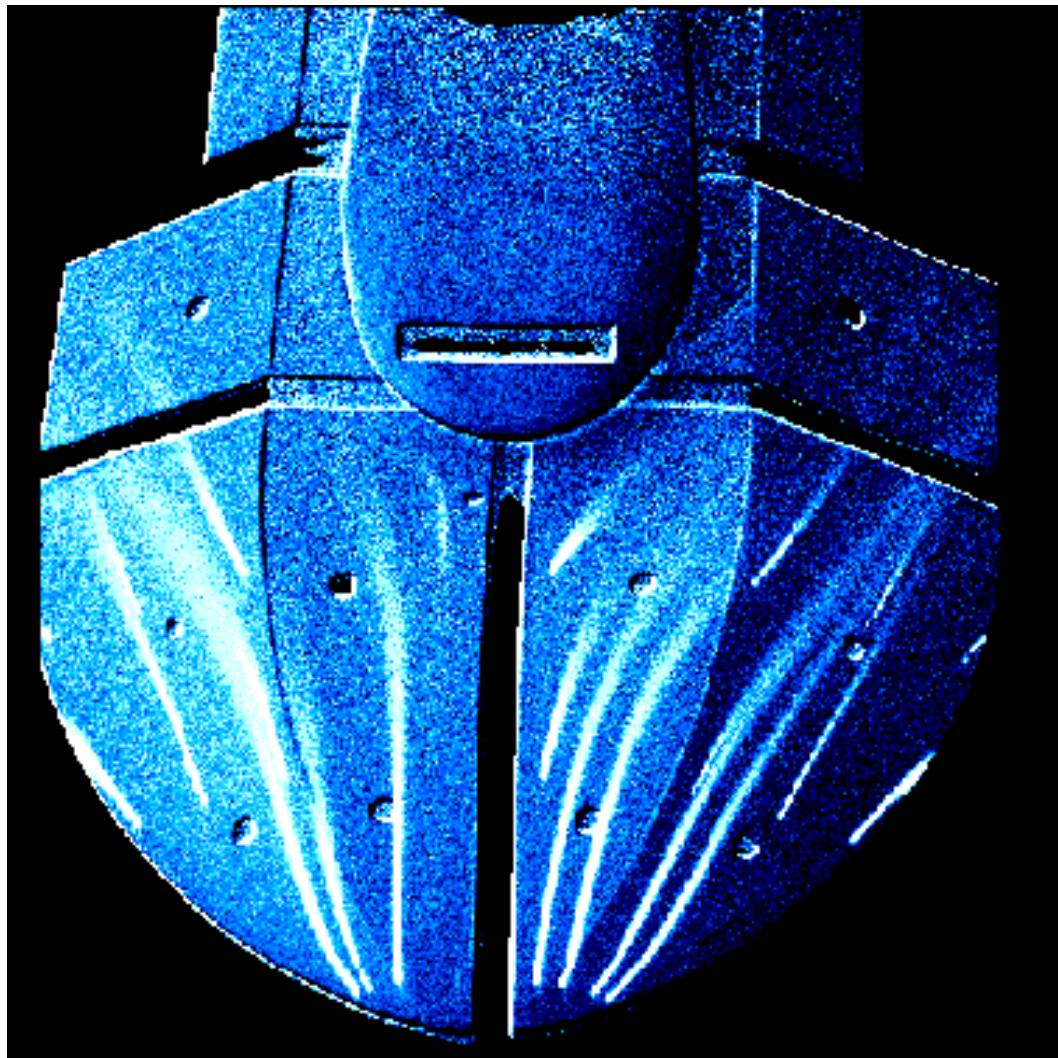
Fig 33. Nitrogen tracer image of streak lines on the Hex body, rotor on, at 36 KTAS
$\alpha=\beta=0.0.$
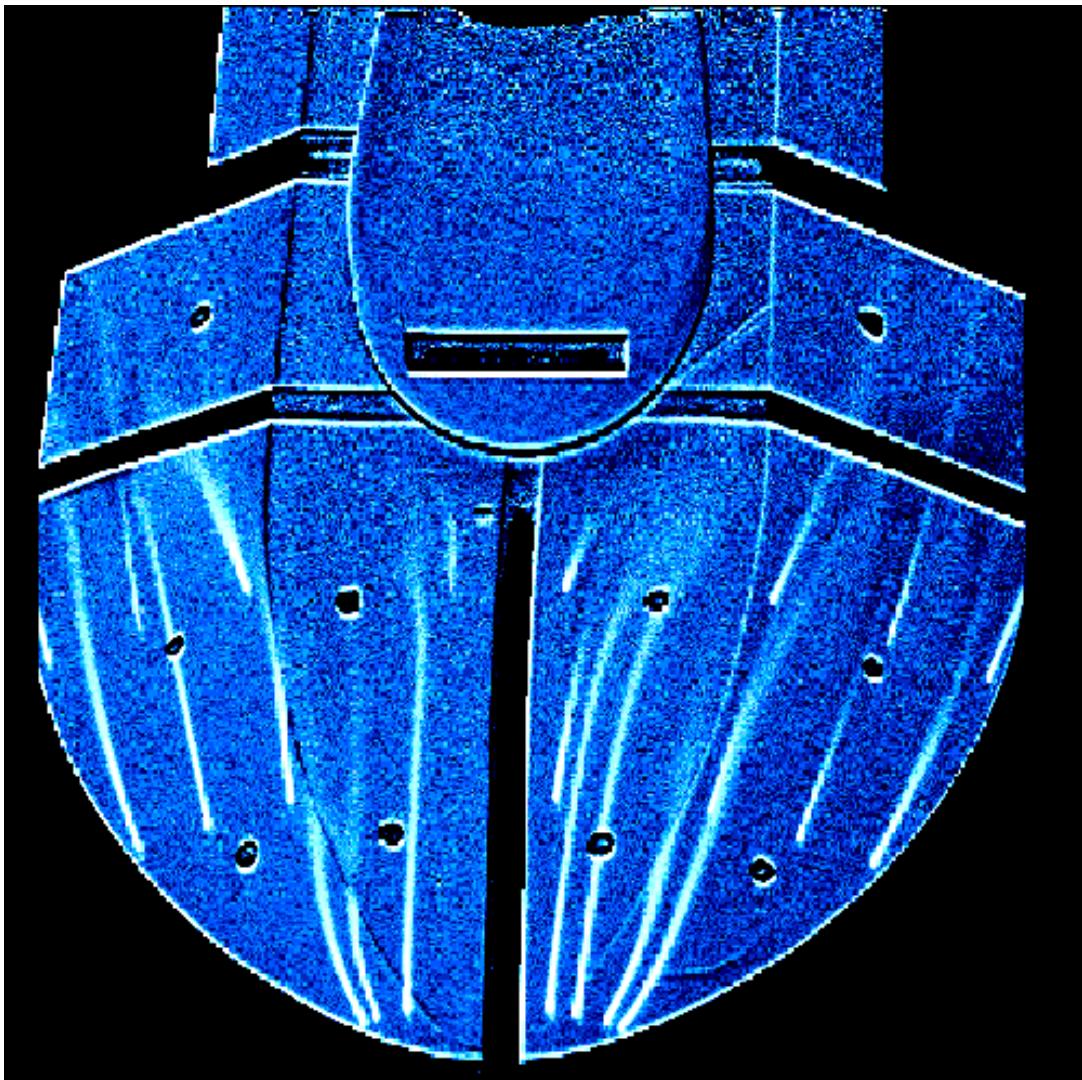
Fig 34. Nitrogen tracer image of streak lines on the Hex body, rotor on, at 60 KTAS
$\alpha=\beta=0.0$.
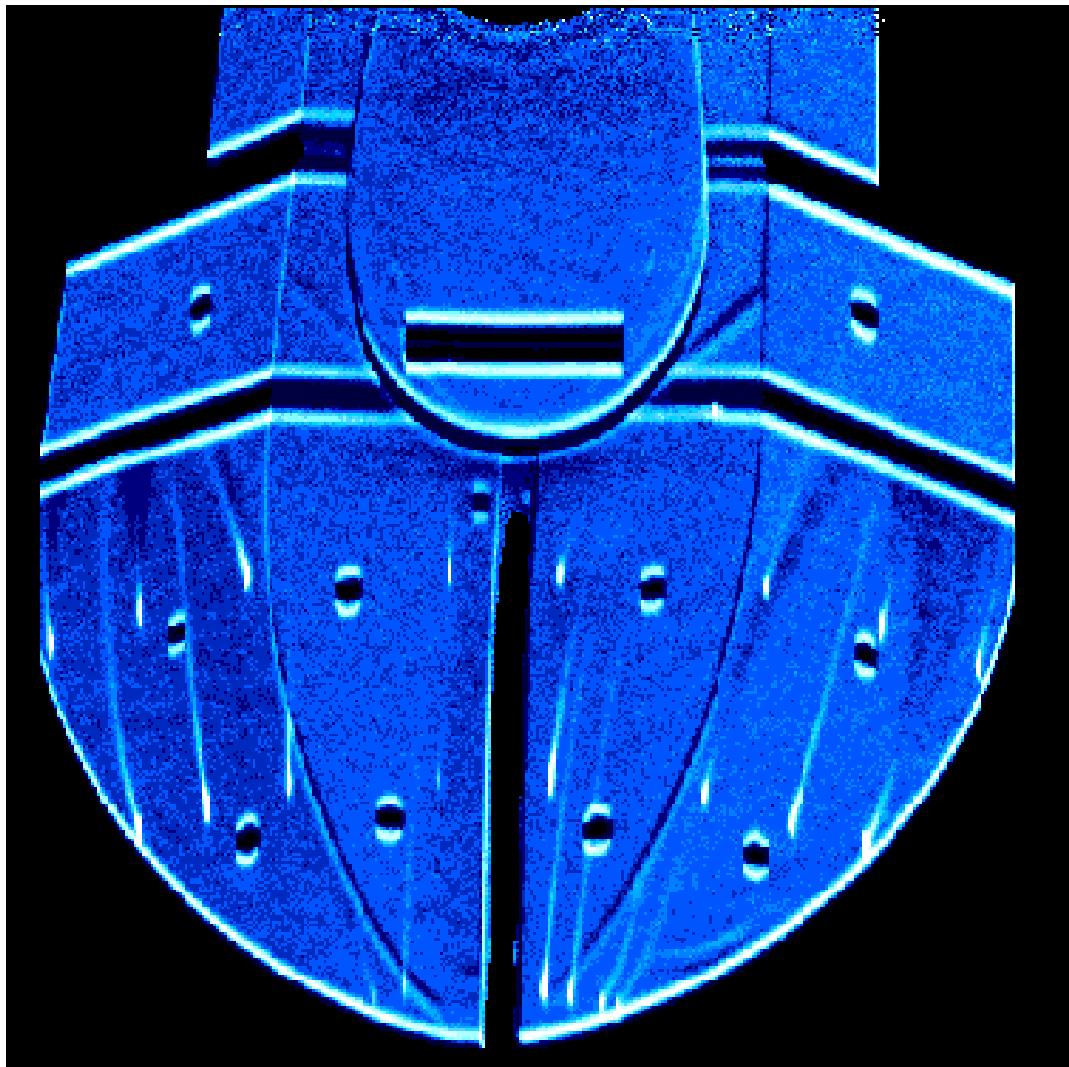
Fig 35. Nitrogen tracer image of streak lines on the Hex body, rotor on, at 136 KTAS $\alpha=\beta=0.0$.